remote sensing

MDPI

Article

Detecting Coseismic Landslides in GEE Using Machine Learning Algorithms on Combined Optical and Radar Imagery

Stefan Peters [1,*], Jixue Liu [1], Gunnar Keppel [1], Anna Wendleder [2] and Peiliang Xu [3]

[1] Unit of Science, Technology, Engineering and Mathematics (STEM), University of South Australia, Mawson Lakes, SA 5095, Australia; jixue.liu@unisa.edu.au (J.L.); gunnar.keppel@unisa.edu.au (G.K.)
[2] German Remote Sensing Data Center, German Aerospace Center (DLR), 82234 Weßling, Germany; anna.wendleder@dlr.de
[3] Disaster Prevention Research Institute (DPRI), Kyoto University, Kyoto 611-0011, Japan; pxu@rcep.dpri.kyoto-u.ac.jp
* Correspondence: stefan.peters@unisa.edu.au; Tel.: +61-8-830-25245

Abstract: Landslides, resulting from disturbances in slope equilibrium, pose a significant threat to landscapes, infrastructure, and human life. Triggered by factors such as intense precipitation, seismic activities, or volcanic eruptions, these events can cause extensive damage and endanger nearby communities. A comprehensive understanding of landslide characteristics, including spatio-temporal patterns, dimensions, and morphology, is vital for effective landslide disaster management. Existing remote sensing approaches mostly use either optical or synthetic aperture radar sensors. Integrating information from both these types of sensors promises greater accuracy for identifying and locating landslides. This study proposes a novel approach, the ML-LaDeCORsat (Machine Learning-based coseismic Landslide Detection using Combined Optical and Radar Satellite Imagery), that integrates freely available Sentinel-1, Palsar-2, and Sentinel-2 imagery data in Google Earth Engine (GEE). The approach also integrates relevant spectral indices and suitable bands used in a machine learning-based classification of coseismic landslides. The approach includes a robust and reproducible training and validation strategy and allows one to choose between five classifiers (CART, Random Forest, GTB, SVM, and Naive Bayes). Using landslides from four different earthquake case studies, we demonstrate the superiority of our approach over existing solutions in coseismic landslide identification and localization, providing a GTB-based detection accuracy of 87–92%. ML-LaDeCORsat can be adapted to other landslide events (GEE script is provided). Transfer learning experiments proved that our model can be applied to other coseismic landslide events without the need for additional training data. Our novel approach therefore facilitates quick and reliable identification of coseismic landslides, highlighting its potential to contribute towards more effective disaster management.

Keywords: landslide detection; satellite remote sensing; machine learning; classification; Google Earth Engine; transfer learning

Citation: Peters, S.; Liu, J.; Keppel, G.; Wendleder, A.; Xu, P. Detecting Coseismic Landslides in GEE Using Machine Learning Algorithms on Combined Optical and Radar Imagery. *Remote Sens.* **2024**, *16*, 1722. https://doi.org/10.3390/rs16101722

Academic Editors: Valerio Tramutoli, Francesco Marchese, Nicola Genzano and Carolina Filizzola

Received: 9 April 2024
Revised: 7 May 2024
Accepted: 10 May 2024
Published: 13 May 2024

1. Introduction—Context and Related Work

Landslides occur when a slope equilibrium is disturbed, causing downslope movement of soil, rock, and organic materials under the effects of gravity. They may be triggered by seismic activities, heavy rainfall, volcanic eruptions, or ground cover changes and can cause widespread damage to landscapes, infrastructure, and human lives and livelihoods [1,2]. It is therefore important to detect landslides accurately and quickly and this study proposes a remote sensing (RS) approach to do this using earthquake-triggered landslides as case studies.

1.1. Earthquakes and Coseismic Landslides

Earthquakes are ranked among the most devastating natural disasters [3] and have caused about 750,000 deaths globally in the last 20 years [4]. The magnitude, intensity, and duration of an earthquake play crucial roles in determining the level of destruction and harm they inflict. The damage is usually generated by earthquake-triggered disasters, including ground shaking, ground rupture, liquefaction, landslides, tsunamis, and floods [5]. Additionally, the specific location and timing of these events also significantly influence their impacts. For instance, the "Tohoku Earthquake" and subsequent earthquakes in Fukushima in 2011 led to 18,426 casualties (confirmed dead and missing), about one million destroyed buildings, and economic costs totaling USD 300 billion [6].

Landslide size or extent, and its impact, primarily depend on the type of landslide, the underlying topography (slope, aspect, elevation, surface curvature, and roughness), and its cause [7]. Both rainfall and seismic activity are primary causes of landslide occurrences [8]. Rainfall-induced landslides typically occur in regions prone to heavy precipitation, especially in areas with steep slopes and poorly consolidated soil or rock. They are triggered primarily by water infiltration and saturation and occur typically during or shortly after heavy rainfall events. Coseismic landslides often occur on landslide-prone slopes or along fault lines where the ground is already weakened. They are directly triggered by seismic shaking and occur immediately or shortly after an earthquake. When seismic and heavy rainfall events co-occur, it is challenging to identify the primary cause [9,10]. In the event of an earthquake, coseismic ground deformation, and distance to the surface rupture zone are important influencing factors of landslide susceptibility [11]. In addition, landslide susceptibility models often take into account landslide conditioning factors such as the amount of rainfall that triggered the landslide event, indices derived from a Digital Elevation Model (DEM) including the topographic wetness index (TWI) and the sediment transport index (STI), as well as spectral vegetation indices such as the Normalized Difference Vegetation Index (NDVI) indicating vegetation density and health [12,13].

1.2. Satellite Remote Sensing-Based Landslide Detection

Detecting landslides using satellite RS-based solutions provides crucial information and evidence for landslide- and earthquake-related research. Landslide detection time, location, and spatial extent of identified landslides, together with information about changes in land surface materials, are not only important for landslide risk/susceptibility modeling, and for disaster impact assessment [14], but also for early disaster response and monitoring. Captured satellite imagery available as near real-time (NRT) products with latency below three hours [15,16], together with effective cloud-based imagery processing and distribution of detected landslide locations to emergency response systems, are key to early response and can save lives and reduce damage.

Multiple relevant satellite imagery sensors for earthquake applications have been identified [17]. RS-based landslide detection approaches utilize both, optical sensors (e.g., Landsat-8 (L8), Sentinel-2 (S2)), and radar sensors (e.g., Sentinel-1 (S1), PALSAR-2 (P2)), as well as elevation and slope raster datasets, usually derived from SAR (synthetic aperture radar) acquisitions by interferometric synthetic aperture radar (InSAR) [18]. Most SAR-based landslide detection methods utilize InSAR to quantify ground surface deformation through measured changes in radar phase between two (pre- and post-landslide event) acquisitions [19,20]. Alternatively, SAR radar backscatter intensity and coherence can also be used to detect changes in ground surface properties due to higher surface roughness of the landslides in the post-event scene leading to higher surface backscattering or due to surface changes (e.g., land cover, roughness, dielectric properties) during pre- and post-event causing a loss of coherence.

While SAR can inform about local surface deformation and surface changes, optical sensors provide useful spectral information. Processing and analysis of relevant satellite imagery for investigating earth surface properties is generally performed by utilizing spectral indices or image classification [21]. Both approaches focus on mapping changes or

the absence of vegetation resulting from landslides. For change detection, a continuous time series of imagery data, including pre- and post-landslide events, is required [22]. When processing optical satellite imagery, cloud pixels can be avoided or reduced by mosaicking of quality-filtered multi-temporal images [23].

Several reviews have discussed and compared satellite RS-based methods for landslide detection [24–28]. In summary, most existing techniques apply a spectral index threshold (e.g., NDVI, rdNDVI (Relative Different NDVI), BSI (Bare Soil Index)), supervised image classification, or radar phase and backscatter change to an imagery obtained from a single satellite sensor. Many methods incorporate slope data at the pixel level into their algorithms, and several approaches involve masking out pixels that fall below a specified slope threshold, thereby eliminating them from consideration as potential landslide pixels. In [29] for instance, a slope threshold of 15 degrees was applied for masking.

Some methods also consider principal component analysis (PCA), which transforms multiple spectral bands acquired at different times into distinct linear components, which results in noise reduction and removal of redundant information in the data, ultimately enhancing the distinction between spectral bands [30,31]. An overview of existing studies is provided in Table 1.

The Sudden Landslide Identification Product (SLIP) [32] algorithm is widely used for landslide detection. It is a multi-sensor approach that explores changes using four thresholds: (1) increases in red wavelength band to signify the exposure of bare earth; (2) variations in the shortwave infrared (SWIR) bands to indicate changes in soil moisture; (3) steep slopes, determined from DEM, to restrict the detection process to areas with pronounced topographic inclines; and (4) s land cover mask to minimize errors of commission specifically within recognized agricultural regions. SLIP was developed for MODIS and L8 imagery, adapted by integrating the inverse NDVI to assess the soil bareness (aSLIP) [33], and improved to utilize S2 instead of L8 imagery (iSLIP) [34]. In addition, Zhang, et al. [35] discussed the potential presence of "old landslides"—areas of previously triggered landslides that did not (fully) recover at the time of the new incident. Such "old landslides" could be falsely detected as new landslides but can be masked to avoid detecting them as false positives (FP), if spatial data about the boundaries of such former landslides are available. Previous studies detecting landslides based on S2, L8, or similar multispectral optical sensors utilized in most cases Level-2A surface reflectance (SR) products, and in a few cases Level-1C Top of Atmosphere (TOA) products [36,37].

Although SR products are generally preferred for land cover classification due to the reduced variability of atmospheric conditions, TOA satellite imagery products can facilitate quicker landslide detection because they are usually available earlier than derived atmospherically corrected SR products. Furthermore, TOA products maintain radiometric consistency across different scenes and can therefore simplify analysis across different images and time periods. Preserving the original spectral information captured by the satellite sensor, TOA products also offer greater flexibility compared to SR products [21]. For instance, different atmospheric corrections can be applied and compared, or TOA products can be utilized without the influence of atmospheric effects, which is valuable for long-term monitoring and trend analysis of land surfaces, including detecting subtle changes indicative of potential landslides.

Validating the accuracy of landslide detection approaches is usually based on available ground truthing, in the form of either point samples of confirmed landslide locations or polygons representing their spatial boundaries. The latter is either captured in the field or created via digitization from very high-resolution (VHR) aerial or satellite RGB imagery on which the boundaries of landslides are clearly visible. Ground truthing-based accuracies assessment utilizes confusion matrix-derived metrics that can be categorized into three groups: (a) metrics on the positive class: recall, precision (Prec), F1 score (F1S), false positive rate (FPR), commission error (CE); (b) metrics on the negative class: specificity (Spec), negative predictive values (NPV), omission error (OE); and (c) metrics on both

classes for imbalanced data: overall accuracy (OA), balanced error (BE), balanced accuracy (BA), quality percentage (QP), and kappa coefficient [38–40].

The accuracies of published landslide detection methods (Table 1) are challenging to compare because they strongly depend on detection and validation methods used, imagery pixel resolution, reliability of ground truthing data, and the study area size. For a reliable comparison, the methods would need to be implemented and applied to the same landslide events while using a comprehensive and accurate ground truthing dataset for validation. With regard to reported accuracies, existing landslide detection methods (Table 1) produced good, but not excellent, detection rates with most accuracies being between 55% and 75%. Combining different optical and SAR imagery while applying advanced machine learning-based models could further improve landslide detection accuracies [28].

Table 1. Comparison of published approaches using satellite imagery for landslide detection. Information about the satellite sensor source, detection method, and study location is provided. "Change detection" indicates whether images pre- and post- ("yes") or only post- ("no") landslide events were utilized. "GEE" indicates whether a method was implemented using Google Earth Engine. "Coseismic" indicates whether case studies used include coseismic landslides or not.

No.	Publication	Satellite Sensors	Detection Method	Change Detection	GEE	Study Area	Co-Seismic
M1	[41]	L8, SRTM DEM	ΔNDVI, Supervised classification	Yes	Yes	Nepal	Yes
M2	[42]	S2, SRTM DEM	ΔNDVI or rdNDVI	Yes	Yes	Sulawesi	Yes
M3	[43]	S2, L8	rdNDVI	Yes	Yes	Papua New Guinea, Kenya	Yes [1]
M4	[40]	S2	ΔBSI	Yes	No	Central America	Yes
M5	[29]	S2, DTM (5 m)	ΔNDVI, slope	Yes	Yes	Italy	No [1]
M6	[31]	S2, ALOS GDEM	Unsupervised classification (NDVIpost, slope, S2post bands)	No	No	India, China, Taiwan	Yes [1]
M7	[38]	S2, ALOS GDEM	Supervised OBIA (NDVIpost, slope)	No	No	India, China, Taiwan	No [1]
M8	[44]	L8	Supervised classification (NDWIpost, NDVIpost, DEM, slope)	No	Yes	India	No [1]
M9	[45]	S1 or S2	ΔNDVI, SAR backscatter (VV-VH)	Yes	Yes	Norway	No [1]
M10	[19,46]	S1	ΔSAR backscatter (VH), heatmap for visual landslide interpretation	Yes	Yes	Haiti; Vietnam; Japan: Hokkaido, Hiroshima;	Yes [1]
M11	[47]	S1	ΔSAR backscatter (VV-VH)	Yes	No	Mexico	Yes
M12	[39,48]	P2	ΔSAR backscatter (HH)	Yes	No	Japan: Hokkaido	Yes
M13	[32]	L8	SLIP (%RedChange, ΔmNDMI)	Yes	No	Nepal, Cameron	Yes [1]
M14	[33]	L8	aSLIP (mRedChange, ΔiNDVIn, ΔmNDMI)	Yes	No	Nepal, Cameron	No [1]
M15	[34]	S2	iSLIP (mRedChange, ΔmNDMI)	Yes	No	Japan: Hokkaido	Yes
M16	[36]	S1, S2	ΔSAR backscatter (VV) or SLIP (%RedChange, ΔmNDMI)	Yes	No	India	No
M17	[49,50]	GE RGB imagery	ML: RetinaNet, YOLO v3, Mask R-CNN, YOLOX	No	No	China	Yes

[1] Case studies include landslides triggered by floods or other weather events.

1.3. Cloud-Based Processing, Google Earth Engine and Machine Learning

Cloud-based satellite imagery processing offers numerous benefits. It enables seamless data integration and interoperability by easily combining satellite imagery with other data sources using standardized application programming interfaces. This allows for smooth integration into existing workflows and software applications. It ensures accessibility and scalability, as large volumes of satellite imagery can be processed and analyzed without the need for additional hardware or infrastructure. This eliminates the cost and maintenance associated with expensive equipment, making satellite image analysis more cost-effective and efficient. Moreover, cloud-based processing provides advanced capabilities for satellite imagery analysis, utilizing machine learning algorithms, computer vision techniques, and Artificial Intelligence tools [51]. These enable researchers to extract valuable insights and patterns from imagery data, uncovering hidden relationships and trends for more accurate and sophisticated analysis.

Furthermore, cloud-based processing enables (near) real-time analysis, crucial for time-sensitive scientific investigations and monitoring applications. It allows researchers to leverage satellite imagery as soon as it becomes available, enhancing the timeliness of their research. Additionally, cloud-based platforms facilitate easy project collaboration, providing a centralized and accessible environment for researchers to collaborate, share data, and work collectively on projects. This promotes interdisciplinary research and knowledge exchange, and accelerates scientific progress. Lastly, cloud-based processing ensures data backup, guarantees data integrity, and reduces the risk of data loss [52].

One prominent and freely available example of a cloud-based processing environment is Google Earth Engine (GEE), which allows users to visualize and process multi-petabyte archives of satellite imagery and geospatial datasets with planetary-scale analysis capabilities. GEE offers support tools to analyze and monitor environmental properties on a large scale [53]. A rise in published journal articles related to GEE over the last three years highlights the increased popularity of GEE, with L8 and S2 being the most widely used earth observation satellite sensors, and articles based on Random Forest and water resources most often reported [54]. Several existing landslide detection methods have been implemented in GEE [19,29,39,42–46,55]. However, only Handwerger et al. [19] provide a shared GEE script that allows replication and potential adjustment of the script to other landslide events. GEE offers not only the opportunity to implement and compare existing landslide detection methods but also to apply and compare different ML classifiers for advanced landslide detection, an aspect that to our knowledge has not yet been addressed in the literature. In addition to detection, a few other landslide-related studies implemented in GEE are worth noting, focusing on landslide deformation tracking [56], recovery [37], or susceptibility [57–60]. Khan, et al. [61] provide a comprehensive comparison of all ML classifiers available in GEE (except Gradient Tree Boost (GTB)). The only published research using ML algorithms in GEE for landslide detection that we are aware of is based on RGB satellite imagery extracted from Google Earth Pro [49,50].

1.4. Research Gaps, Aim and Contributions of This Work

In summary, the following research gaps for RS-based landslide detection have been identified:

- Existing methods built upon change detection of either spectral index or SAR backscatter, but the benefits of combining optical and SAR sensor bands have not yet been explored;
- No study has applied and compared the performance of different ML classifiers available in GEE for landslide detection;
- Existing studies using optical sensors (e.g., L8 or S2) have used SR products, but none have investigated the use of TOA vs. SR products regarding resulting landslide detection performance;
- No comparison of existing landslide detection methods has been applied to the same study dataset;

- No study has investigated the benefits of transfer learning for landslide detection;
- No ready-to-use ML-based solution to landslide detection is available in GEE.

The main aim of our work is to utilize ML algorithms and image fusion within GEE to improve RS-based landslide detection. Specifically, the following research questions will be addressed in this paper:

- To what extent could ML-based landslide detection using stacked bands from multiple optical and radar sensors improve landslide detection compared to existing approaches?
- How do ML classifiers, available in GEE and applied to landslide detection, compare in terms of performance and processing speed?
- What are the possibilities in GEE for early landslide detection—how does the use of TOA radiance products compare to SR products?
- How important are relevant spectral and derived topographic bands for landslide detection?
- What other factors impact satellite imagery-based landslide detection accuracy?
- To what extent can an ML-based landslide detection in GEE be fully automized to allow easy operational adjustment to any spatio-temporal scenario?

With the purpose of addressing these research questions and research gaps, our work will provide the following contributions:

- Detailed comparison of the performance (accuracy assessment) of existing RS-based landslide detection methods using ground truthing datasets from four different case sites;
- Novel RS-based landslide detection solution that:
    - Utilizes stacked multi-band optical and SAR imagery at 10 m spatial resolution including S1, S2, P2, and elevation-derived topographic bands;
    - Applies landslide-specific training and validation sampling strategy based on a novel slope masking approach;
    - Applies ML classifier with optimized parameters to boost performance and processing speed;
    - Utilizes new additional pseudobands as part of the ML classifier: slope curvature, aspect, P2 SAR bands, S1 SAR band: combined VH-VV;
    - Is implemented in GEE with an accessible source code, including landslide inventory data for all four study sites and a guideline to adjust the GEE code to any study area;
- Investigation of the importance of each landslide conditioning band within the ML model;
- Thorough investigation and comparison of ML classifiers in GEE for coseismic landslide detection;
- Comprehensive across-geography applied transfer learning-based landslide detection and validation;
- Transfer learning space transferability.

Hence, our novel approach provides a significant contribution to RS-based landslide detection, which we illustrate using four different case studies on coseismic landslides caused by 6.6–7.5 magnitude earthquakes that occurred across the globe between 2016 and 2021. The remaining content of this manuscript is structured as follows: Section 2 introduces the study area, provides details on the satellite imagery datasets used, and explains in detail the workflow of our proposed approach that includes multi-sensor imagery fusion, ML-based landslide detection, experimental settings, and used evaluation metrics. Section 3 will present the results and Section 4 will discuss the results and provide insights into the detection accuracies of existing solutions compared to our solution; discuss the performance of different ML classifiers; explain the importance of each sensor band; compare TOA vs. SR as part of the detection solution; discuss space transferability; present the conclusion and explore future possibilities.

2. Materials and Methods

2.1. Case Studies

Below, four coseismic earthquake case studies used in this paper are described. Table 2 provides an overview of each event, including details of the sourced landslide inventory data. Figure 1 maps these inventory data and the used study area boundaries.

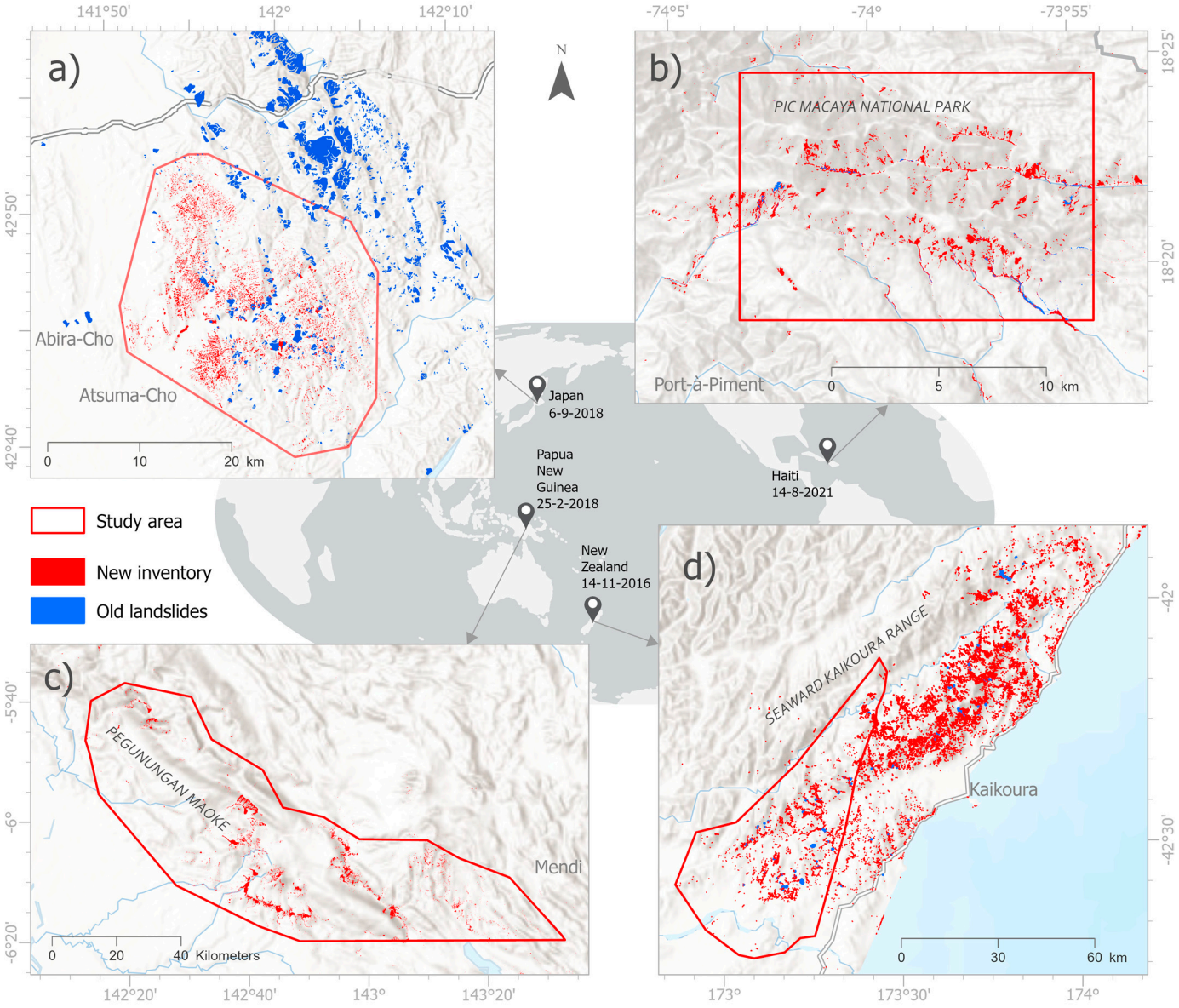

Figure 1. Distribution of landslides recorded in the landslide inventories used as case studies in (**a**) Japan, (**b**) Haiti, (**c**) Papua New Guinea, and (**d**) New Zealand, and study areas implemented in this study. The distribution of coseismic (old and new) landslides based on available landslide inventory data is indicated.

Table 2. Coseismic landslide inventories used as case studies in this paper. Information about the landslide location, human fatalities and injured, and the inventory approach (methodological approach, number of landslides inventoried, and spatial extent) are provided.

Earthquake Date	Epicenter Location	Epicenter Lat/Lon	Focal Depth (km)	M_w, Death, Injured	Inventory Method	Ref.	No. Inventory Landslides	Used Landslides	Study Area (km^2)
6 September 2018	Japan, Hokkaido, Iburi	42.662°N 142.011°E	37	6.6, 41, 691	VHR UAV imagery, PlanetScope	[62]	5625	5208 (93%)	359
14 August 2021	Haiti, Tiburon Peninsula, Pic Macaya NP	18.434°N 73.482°W	10	7.2, 2200, 12,200	GE imagery, PlanetScope	[63]	6100	80%	170
25 February 2018	PNG, Hela Province, Komo	6.070°S 142.754°E	15–30	7.5, 160, 500	GE imagery, PlanetScope, Rapid Eye	[64]	11,607	8912 (77%)	5163
14 November 2016	New Zealand, South Island, Kaikōura	42.737°S 173.054°E	15	6.7, 2, 618	GE imagery, S2	[65]	14,233	2521 (18%)	1370

2.1.1. Japan, 2018 M_w 6.6 Hokkaido Earthquake

On 6 September 2018, a moment magnitude 6.6 earthquake struck the Iburi Subprefecture in Southern Hokkaido, Japan, following Typhoon Jebi's passage. The 2018 Hokkaido Eastern Iburi earthquake is hereafter referred to as "JPN case study". Aftershocks indicated compression along the ENE-SWS direction in the Northern, Southern, and Shallow Iburi faults [66]. The earthquake caused extensive damage, triggering thousands of landslides. A comprehensive inventory map identified nearly 6000 coseismic landslides, mostly small to medium translational ones with high mobility and long run-out distances ranging from 25 m^2 to up to 57,000 m^2. This dataset, representing ground truth polygons of all landslides triggered during the 2018 Hokkaido earthquake, is hereafter referred to as "landslide inventory". The spatial extent of the study area was defined by applying a convex hull around the landslide inventory polygons, resulting in an extension of 22 km (east–west) by 24 km (north–south) geodetic distance, while the convex hull-shaped study area spans a geodetic area of 359 km^2. Note that for computational reasons, a few distant/isolated landslide inventory polygons were excluded to reduce the total study area. Despite the area's low population density (less than 10 persons per km^2), the landslides resulted in 41 fatalities and 691 people injured. The landslide concentration formed an elliptical area parallel to the region's (active) faults, with the most affected aspect being southerly, perpendicular to the NNW/SSE striking faults. These coseismic landslides occurred in regions with a seismic intensity ranging from 7.0 to 8.0 on the Modified Mercalli intensity scale and peak ground acceleration between 0.4 and 0.7 g. They were densely distributed in hilly regions at elevations between 100 and 250 m, with slope angles ranging from 15° to 35°. Most of the landslides were shallow, several meters deep, and categorized as planar and spoon types [67]. The area predominantly consists of Neogene sedimentary rocks overlaid by pumice layers from Tarumai volcano to the east. Surface soil layers in the low to middle mountain ranges contain interbedded pumice and ash, with a thickness of approximately 4–5 m [39]. The landslide-prone area primarily consists of Miocene sedimentary rock. Slope failures occurred in stratified pyroclastic fall deposits due to a combination of strong seismic ground motion and intense antecedent precipitation [35].

2.1.2. Haiti, 2021 Tiburon Peninsula M_w 7.2 Earthquake

On 14 August 2021, a seismic event of moment magnitude 7.2 struck the region of Nippes, Haiti, specifically on the Tiburon Peninsula, marking a significant geological event. This seismic disturbance was attributed to activity along the Enriquillo–Plantain Garden Fault, a seismogenic fault renowned for its tectonic significance in the area. The aftermath of this earthquake revealed a notable impact on the landscape, triggering over 8444 landslides

across an expanse of approximately 2700 km^2. Among these, an area totaling 45.6 km^2 experienced direct landslide activity, with particular concentration observed in the western region of the Tiburon Peninsula. Notably, the Pic Macaya National Park emerged as a focal point, with approximately 6100 landslides occurring within or near its confines, constituting 72.2% of the total landslide occurrences, hereafter referred to as "HTI case study". Further analysis revealed that 89.4% of the landslides were predominantly situated in the hanging wall area and regions characterized by high relief, featuring slopes ranging between 35° and 55° [63]. The consequences of these landslides were multifaceted, directly resulting in fatalities and extensive damage to infrastructure. Moreover, the obstruction of roads and other vital pathways hindered response efforts, exacerbating the challenges faced in the wake of this seismic event [68].

The spatial extent of the study area was defined by applying an envelope around the landslide inventory polygons, resulting in an extend of 16 km (east–west) by 11 km (north–south) geodetic distance, while the convex hull-shaped study area spans a geodetic area of 170 km^2. Note that for computational reasons, a few distant/isolated landslide inventory polygons were excluded to reduce the total study area.

2.1.3. Papua New Guinea, 2018 M_w 7.5 Earthquake

In the highlands of Central Papua New Guinea (PNG), close to Komo in the Hela Province, a seismic event of moment magnitude 7.5 took place on 25 February 2018. This event, hereafter referred to as "PNG case study", stands as the most remarkable earthquake documented within this geographical expanse over the preceding century. Subsequently, the affected area experienced four substantial aftershocks (each with a moment magnitude equal to or exceeding 6.0) within a span of 9 days following the mainshock. The affected area is highly susceptible to landslides due to its climatic, geologic, and tectonic influences. Furthermore, local environmental conditions serve to amplify the seismic shaking, exacerbating the propensity for landslides. The aftermath of the seismic event was characterized by a huge amount of landslides throughout the region [69].

The initial earthquake and its ensuing aftershocks triggered widespread landslides, with an estimated total exceeding 11,600, of which >10,000 were triggered by the principal earthquake. These landslides collectively generated a cumulative planimetric failure area encompassing approximately 145 km^2. Steep hillslopes caused the activation of large landslides reaching dimensions of up to approximately 5 km^2 for single landslides. Analysis of the seismic event delineated a predominant reverse fault motion, with discernible displacement reaching up to approximately 0.7 m along faults extending to depths surpassing 25 km [64].

The spatial extent of the study area was defined by applying an envelope around the landslide inventory polygons, resulting in an extend of 148 km (east–west) by 84 km (north–south) geodetic distance, while the convex hull-shaped study area spans a geodetic area of 5163 km^2. Note that for computational reasons a few distant/isolated landslide inventory polygons were excluded to reduce the total study area.

2.1.4. New Zealand, 2016 M_w 6.7 Kaikōura Earthquake

On 14 November 2016, the Northeastern South Island of New Zealand experienced a seismic event of M_w 7.8 known as the Kaikōura earthquake. This earthquake, hereafter referred to as "NZL case study", exhibited a remarkably intricate rupturing mechanism, unprecedented in complexity within recorded seismic activity. The seismic instrumentation in place within the region provided comprehensive data on the event. A total of 14,233 landslides were documented, covering an extensive area of approximately 14,000 km^2. The earthquake's rupture sequence impacted a series of active faults, extending offshore and significantly affecting coastal and inland areas across the northeastern part of the South Island.

Analysis of global moment tensor solutions revealed the intricate nature of this multi-fault rupture earthquake. The rupture process was observed to propagate from south to

north, establishing connections between the Hikurangi subduction system of the North Island and the oblique collisional regime of the South Island, notably the Alpine Fault. The impacts of the Kaikōura earthquake on both infrastructure and the environment were severe and widespread. Reconstruction efforts were estimated to cost between NZD 3 and 8 billion, underscoring the scale of the challenges posed by the event's aftermath [65].

The spatial extent of the study area was defined by applying an envelope around the landslide inventory polygons, resulting in an extend of 48 km (east–west) by 69 km (north–south) geodetic distance, while the convex hull-shaped study area spans a geodetic area of 1370 km^2. Note that for computational reasons a few distant/isolated landslide inventory polygons were excluded to reduce the total study area.

2.2. Methodology

As illustrated in Figure 2, Our ML-LaDeCORsat approach involved two principal steps: (a) preprocessing and (b) training and evaluation of an ML algorithm used to classify a combined S2 optical S1 SAR imagery dataset into landslide and non-landslide pixels.

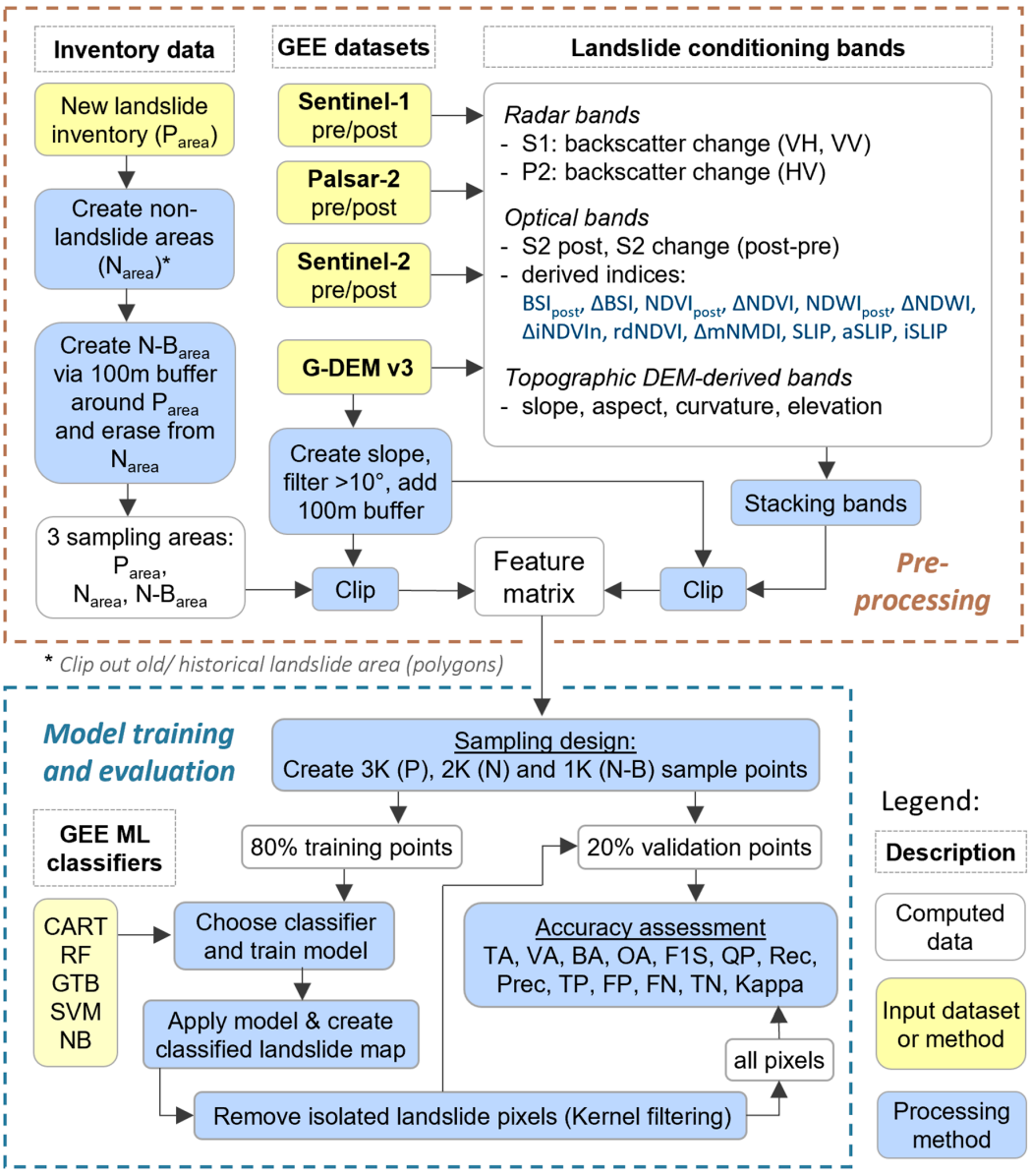

Figure 2. Conceptual overview of the ML-LaDeCORsat approach. The approach involves two principal steps: pre-processing (**top box**) and model training and evaluation (**bottom box**).

2.2.1. Data Preparation

Considering previous approaches (see Table 1), several satellite sensors and imagery bands that are available in GEE are relevant for landslide detection as proposed in this work (Table 3).

Table 3. Location and content information about satellite imagery bands available in GEE that are relevant to landslide detection. Ground sample distance (GSD) is the distance between two consecutive pixel centers measured on the ground.

Sensor	Bands	GSD (m)	Description and Source (URL)
S2-L1C	B2-B12	10 or 20	Sentinel-2 L1C (TOA) multispectral bands https://developers.google.com/earth-engine/datasets/catalog/sentinel-2 (accessed on 9 October 2023)
S1	VV, VH	10	Sentinel-1 C-band Interferometric Wide swath, Ground Range Detected, log scaling; https://developers.google.com/earth-engine/datasets/catalog/COPERNICUS_S1_GRD (accessed on 9 October 2023)
P2	HH, HV	25	PALSAR-2 L-band ScanSAR Level 2.2 backscatter data, log scaling https://developers.google.com/earth-engine/datasets/catalog/JAXA_ALOS_PALSAR-2_Level2_2_ScanSAR (accessed on 9 October 2023)
ASTER	Elevation (b1)	30	ASTER Global Digital Elevation Model (GDEM) Version 3 https://gee-community-catalog.org/projects/aster/ (accessed on 9 October 2023)

To prepare multispectral S2 data for landslide detection for each case study, two cloud-free sets of imagery covering the entire area of interest (AOI) were necessary, representing the situations before and after the landslide events.

As shown in Figure 1, the inventories of landslides used in this work did not include the entire available inventory source dataset. For GEE performance reasons, a convex hull was applied covering the majority of all inventory data while excluding a small amount of rather isolated inventory landslides. In addition, for the NZL case study, available Sentinel-1 post-event imagery only covered the southeast part of the available inventory data.

Except for the NZL case study, a single S2 imagery scene available in GEE did cover the respective AOI. In the case of NZL, three adjacent cloud-free S2 imagery had to be joined using the GEE *ImageCollection.mosaic()* function.

Due to the likeliness of cloud coverage, it is suggested to compute multi-temporal image composites ("mosaics") [45]. In this work, S2 multi-temporal image mosaics were created for the pre- and post-earthquake scenario over the PNG case study due to significant cloud coverage in all S2 imagery in 2017 and 2018. In total 88 selected S2 imagery during 2017 were used to create a cloud-free S2 pre-earthquake mosaic and 67 selected S2 imagery between March and July 2018 to create a cloud-free S2 post-earthquake mosaic. Due to PNG's geographic location being close to the equator causing its hot, humid climate with all months above 18 °C, seasonal reflectance dynamics have only a marginal impact on these mosaics if at all. For the other three case studies, nearly or completely cloud-free S2 imagery was available within a few months after each earthquake event. A cloud-free pre-earthquake S2 imagery was then extracted approximately one year earlier to avoid seasonal reflectance dynamics.

Since an S2-L1C (TOA) image product can be available (on GEE) up to a few hours earlier than S2-L2A (SR), it was decided to use the S2-L1C product, and to apply, dependent on its impact on landslide detection accuracies, the Sensor Invariant Atmospheric Correction (SIAC) method [70] to convert TOA radiance into estimated SR values in GEE. Masking was applied to the few cloudy pixels in the pre-earthquake S2 image using the S2 QA60 (cloud mask) band. In addition, S2-L1C (TOA) data have been available in GEE since July 2015, and S2-L2A (SR) data only since April 2017, which allowed us to utilize the NZL case study, which occurred in 2016.

Sentinel-1 imagery data accessible via GEE consists of radiometric calibrated, orthorectified SAR C-band backscatter images available in four polarization modes: (1) single co-polarization: vertical transmitting, vertical receiving (VV), (2) single co-polarization: horizontal transmitting, horizontal receiving (HH), (3) dual-band cross-polarization: vertical transmitting, vertical and horizontal receiving (VV and VH), and (4) dual-band cross-polarization: horizontal transmitting, horizontal and vertical receiving (HH and HV). As argued by [19], HH and HV polarizations are less useful for landslide detection, thus only VV and VH polarization were considered due to their sensitivity to forest biomass structure [71].

Due to the longer wavelength, the emitted L-band radar of ALOS-2/P2 can better penetrate through denser vegetation compared to S1's C-band. The GEE-provided orthorectified and radiometrically calibrated and terrain-corrected normalized backscatter data of P2 used in this work, were available as HH and HV polarization bands. The available S1 SAR imagery data included in this study comprised the period of approximately four months before and after the earthquake in order to identify sufficient ascending and descending pre-earthquake, respectively, post-earthquake imagery. Following the approach of [19], the temporal median of the pre-event and post-event SAR data were computed, and ascending and descending data were combined by calculating their mean values.

Due to the differences between S1 and P2 in terms of sensor characteristics, polarimetry, orbit parameters, imaging strategies, and data availabilities in GEE, a much larger time window for P2 had to be selected. Even including all available P2 imagery since 2014 and until the present, sufficient ascending and descending pre- and post-event P2 imagery were only available for the JPN case study. Further details about temporal filtering of the utilized S2, S1, and P2 imagery for all four study sites are provided in Supplementary Table S14.

In addition to using elevation data sourced from ASTER GDEM to extract landslide conditioning factors, slope values derived from the GDEM were used to mask out irrelevant pixels below a certain slope threshold (e.g., 10 degrees). Another potentially relevant conditioning factor is pixel-based solar radiation. However, the only globally available raster dataset in GEE is the Global Solar Atlas, generated using Shuttle Radar Topography Mission (SRTM) derived elevation data combined with MTSAT and Himawari-8 reflectance data as reported in [72]. Due to its coarse spatial resolution of 250 m, the solar atlas was not incorporated into this work.

2.2.2. Landslide Conditioning Factors

As shown in Figure 2, several bands and derived bands ("pseudobands") were identified from literature as relevant landslide conditioning factors—and used in the ML-LaDeCORsat approach. For S2, these include the following bands: (a) all spectral bands of the prepared S2 post-earthquake image except B1 (aerosol), B9 (water vapor), and B10 (cirrus), (b) the differences of each spectral band by subtracting pre-earthquake reflectance values from post-earthquake ones, and c) the below-listed computed spectral indices (prefixes in front of spectral index abbreviation: "Δ" refers to change (post minus pre), "i" refers to inverse, "m" refers to modified, "n" refers to normalized, and "rd" refers to relative difference):

- Soil index: BSIpost, ΔBSI [40];
- Vegetation index: NDVIpost, ΔNDVI, rdNDVI, ΔiNDVIn [31,38,40–45];
- Water index: NDWIpost, ΔNDWI [44];
- Drought index: ΔmNMDI [32,34];
- Sudden Landslide Identification Product/index: SLIP [32], aSLIP [33], iSLIP [34].

Specific index formulas and thresholds can be found in the cited references. All these indices had been used in previous landslide detection methods, except BSI_{post}, which was added to explore its importance for detection performance.

Utilizing S1 polarization bands, the same methodology as suggested in [19] was followed to determine the log ratio (and percentiles of it) for pre- and post-event S1 SAR intensity using different polarizations. It was then decided to include the following three

bands, which were identified via empirical investigation as the best-performing bands for landslide detection:

- S1_log_VH: log ratio for pre- and post-event S1 SAR (VH) intensity;
- S1_90p_VH: 90th percentile of S1 log ratio (VH);
- S1_90p_VH_VV: 90th percentile of S1 log ratio (VH and VV).

Utilizing P2 polarization bands, the same process as for S1 was applied and the following band was identified to be included in the ML classifier used in this study: P2_log_HV, the log ratio for pre- and post-event P2 SAR (HV) backscatter.

Derived from GDEM, the following topographic factors were included: slope, aspect, curvature, and elevation [29,31,38]. These topographic data were derived from imagery taken prior to the earthquake event. Post-earthquake elevation data were not available in this work, but data including detailed changes in elevation might further improve detection results.

Further relevant topographic indices are TWI and STI, computed using slope and flow accumulation as inputs. While slope can be easily created in GEE from a given DEM, GEE does not provide a function to compute flow accumulation out of the box due to a significant amount of required iterative operations. TWI and STI could be, however, computed from a DEM using GIS software and uploaded into GEE. In GEE, available rainfall datasets do not provide the required spatial resolution to be considered for this work. The Global Precipitation Measurement (GPM) dataset [73], for instance, supplies global precipitation estimates updated every 30 min, but only at a spatial resolution of 0.1 degrees (approximately 11 km). As the focus of this work was to produce a replicable and ready-to-use GEE landslide detection product, the use of TWI and STI was not further investigated.

In summary, these identified indices, allowed the proposed ML-LaDeCORsat detection method to address changes in surface vegetation, vegetation moisture, bare soil, soil moisture, and bare-earth exposures derived from S2 imagery; to consider alterations in ground surface properties (e.g., roughness, dielectric properties) through S1 and P2 SAR intensity and coherence changes; and to incorporate topography features of the study area (e.g., slope, aspect) using the GDEM.

In preparation for the image classification, pre-processed SAR and topographic bands were spatially reprojected and resampled to match pixel dimension (10 m) and position of S2 pixels. Next, all 40 landslide conditioning bands were combined into a single image using the *addBands* GEE function. This multi-band stacked image was then fed into the ML feature matrix.

Investigations into PCA bands derived from S2 post and S2 change bands did not lead to improved landslide detection accuracies, for none of the four case studies, hence PCA bands were not included in this work.

2.2.3. ML Sampling Strategy

A sampling strategy specifically designed for ML-based classification of landslides was developed. This strategy consists of several geoprocessing steps, illustrated in the preprocessing part of the provided flowchart in Figure 2. First, three sampling areas were defined. Utilizing the above-mentioned landslide inventories to define a "Positive" sampling area (P_{area}), the GIS Erase tool was applied to generate an initial non-landslide "Negative" sampling area (N_{area}). To allow a stratified random sampling method to create sufficient sampling points near inventoried landslide polygons, a 100 m ring buffer was created around the P_{area}, forming a second "Negative" sampling area: the N-B_{area}. This ring buffer area was also erased from the initial N_{area}. Sampling points inside N-B_{area} allow the model to put emphasis on "border" areas around landslides.

Next, the spatial extent of sampling areas and the multi-band stacked input image were reduced by removing pixels within areas of low slopes, less than 10 degrees. Such slope filtering has been applied in many of the existing RS-based landslide detection approaches, including [29,32–34]. This, however, can cause false positives (FP) for scenarios in which

the landslide is triggered at steeper slopes, but its flow area reaches into areas of lower slopes, as illustrated in Figure 3.

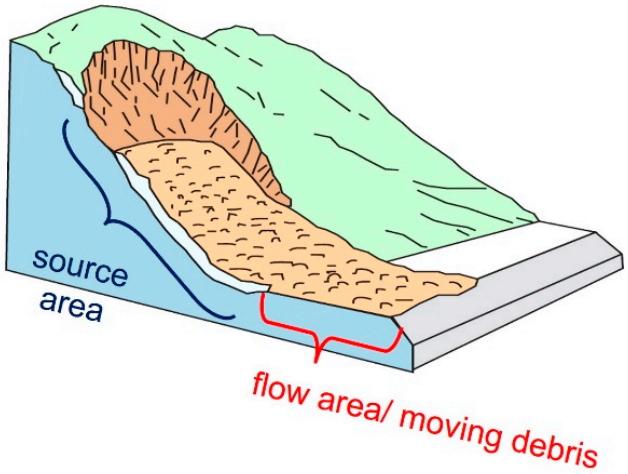

Figure 3. Schematic of a landslide event that illustrates source and flow areas. Adapted from [1], figure 17.

To address this issue, a 100 m buffer was added to the slope filtering (using >10 degrees) before clipping the ML input image with the final sampling areas. The buffer size of 100 m was determined empirically. Not applying such a buffer has a strong impact on causing FP as can be seen in Figure 4. Pixels with slopes >20 degrees are mapped in grey on top of red-color-coded landslide inventory areas. The slope threshold of >10 degrees applied to the JPN case study only overlaps 24% of the landslide inventory polygons (P_{area}). Only when adding the 100 m buffer, more than 99% of the inventory data were covered, as shown in Figure 4b. Table 4 lists landslide inventory areas not covered by a >10 degree slope threshold for all four case studies.

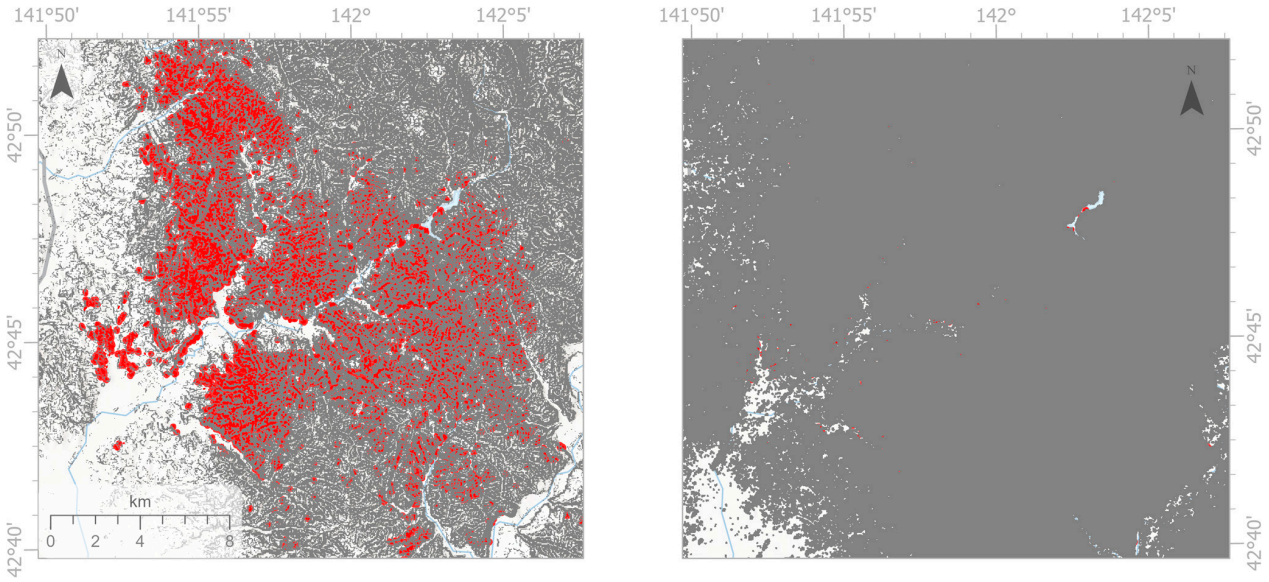

Figure 4. Effect of adding a buffer to slope filtering for the Japan case study. When mapping slope filtering (grey) on top of the landslide inventory (red) with (**a**): slope threshold >10 degrees and (**b**) slope threshold >10 degrees plus 100 m buffer, 24% and 99% of inventoried landslides are covered, respectively.

Table 4. Variation among the four case study sites in the maximum and mean slopes, and the landslide areas covered when implementing 10 degree (10°) slope thresholds.

Site	Slope Max.	Slope Mean	Inventory and Slopes	Area [km^2]	%
JPN	61	19	Inventory area covered by 10°slope	18,240	76%
			Not covered	5753	24%
			Total	23,993	100%
HTI	75	29	Inventory area covered by 10° slope	10,557	95%
			Not covered	567	5%
			Total	11,123	100%
PNG	85	22	Inventory area covered by 10° slope	161,196	87%
			Not covered	23,865	13%
			Total	185,061	100%
NZL	73	24	Inventory area covered by 10° slope	13,145	88%
			Not covered	1787	12%
			Total	14,932	100%

2.2.4. ML Classifier

For ML model training and evaluation, a randomly stratified point sampling approach was implemented using in total 6000 sampling points that consists of 3000 "landslide" points inside P_{area}, 2000 "non-landslide" points inside N_{area}, and another 1000 "non-landslide" points inside N-B_{area}. Each of these three parts was then split into 80% training points and 20% validation points as exemplarily shown in Figure 5.

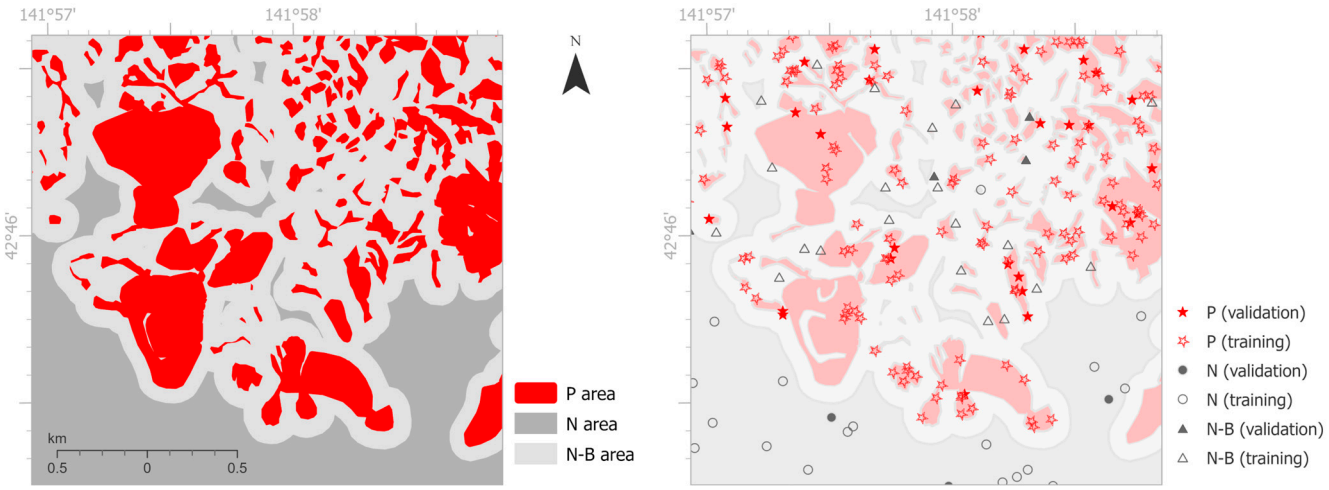

Figure 5. Example of the training and validation approach implemented for the machine learning model. (**a**): Sampling areas with 10 degrees slope and 100 m buffer filter applied were identified as "landslide" inside (P_{area}), "non-landslide" inside (N_{area}), and another "non-landslide" inside N-B_{area}. (**b**): randomly placed training and validation points within each sampling area were assigned at a ratio of 4:1.

Next, all available ML classifiers in GEE were implemented, including Classification and Regression Trees (CART), Naive Bayes (NB), Random Forest (RF), Support Vector Machine (SVM), and Gradient Tree Boost (GTB). For a consistent comparison, a fixed randomization seed with a value of "0" was applied to ensure using the exact same set of randomly distributed sampling points for ML model training and validation. Aiming to compare the performance of all ML classifiers for landslide detection, the optimal settings for the classifiers' parameters were empirically investigated and finally defined as listed in Table 5. Details about GEE classifier and their parameters are described in [74,75]. To further improve detection accuracy, a Gaussian kernel filter (radius: 60 m, sigma: 30) was

applied as suggested in [76] to the classified image to remove wrongly detected isolated single landslide pixels. Older landslides triggered by previous events were excluded from training and prediction. If not considered, the prediction will likely suffer from a high number of FP.

Table 5. Optimal GEE ML classifier parameters for ML-LaDeCORsat.

Classifier	Training Samples	No. of Trees	Min LeafPop [1]	Bag Fraction	Split	Max Nodes	Shrinkage	Sampling Rate
CART	4800	N/A	7	N/A	N/A	40	N/A	N/A
RF	4800	500	7	0.5	10	20	N/A	N/A
GTB	4800	650	N/A	N/A	N/A	20	0.00095	0.173
NB	4800	N/A	N/A	N/A	N/A	N/A	N/A	N/A
Classifier	**No. of Samples**	**Type**	**Kernel Type**	**Decision Procedure**	**Shrinking**	**Degree**	**Gamma**	**Coef0**
SVM	4800	C_SVC	Poly	Margin	TRUE	1	0.5	10

[1] Leaf node's minimum sample value.

2.2.5. Evaluation Metrics

A range of different evaluation metrics were implemented to allow comparison of landslide detection accuracy achieved in this work with existing methods (listed in Table 1). Evaluation metrics used in this study included Kappa, OA, BA, BE, Spec, Recall, Prec, F1S, NPV, OE, CE, FPR, and FNR. Furthermore, pixel counts of TP, FP, FN, and TN were computed and added to the results to allow others to determine any further evaluation metrics, such as omission or commission error. For comparing different classification settings within this work (classifier parameters, sampling input, selected bands, and pseudobands), it was decided to use the BA as one of the main comparative validation metrics due to its advantages for measuring the prediction quality of all target classes as described by [77], along with OA, Recall, Prec, F1S, and Kappa. Moreover, training accuracy (TA) and validation accuracy (VA) were computed to investigate and address potential model overfit (in case of larger differences between TA and VA). Training and validation accuracy of the models are averaged over the five-fold. A detailed description of each metric can be found in [77]. For each case study, the evaluation metrics were computed using approximately 2000 randomly distributed validation points, containing at least 600 points inside landslide inventory polygons. Computing the same evaluation metrics was then repeated considering all pixels of the entire study area. Although a heavier computational task in GEE, the "all-pixel" evaluation approach provides the best possible evaluation.

2.2.6. Band Importance Investigations

When using a set of potentially relevant features or variables (in this case spectral bands or derived indices) for an ML algorithm, it is crucial to investigate the importance of each band to achieve a better insight into what feature contributes towards performance improvement and to decide which features to exclude in order to reduce the classification computation time and memory. In the context of GEE, the classifiers available for importance ranking are limited to decision tree-based models, including CART, GTB, and RF. Decision tree-based models offer robustness against correlations among variables due to the nature of their algorithm. In each step of the decision tree algorithm, only one variable is selected to split the training data, ensuring that correlated predictors are not utilized simultaneously. To investigate the importance of each band, we utilized the GEE inbuilt function: *classifier.explain()* which returns a dictionary that describes the results of a trained classifier and includes band importance factors.

2.2.7. Transfer Learning Investigations

Transfer learning or domain adaptation has been widely used in image classification and other fields [78,79]. It is crucial to note that models predicting landslides may be applied in geographical areas distinct from those where the model's training data were gathered. To verify the performance of ML-LaDeCORsat applied to landslide events, we designed and conducted across-domain transfer learning for each case study with training the ML-LaDeCORsat model using different subsets of target site samples together with the complete sampling point dataset from other case studies. The model was trained on data from one up to three sites and with or without a portion of training data from site four and is applied to the test data of site four for evaluation. Comparing and validation of across domain trained ML-LaDeCORsat outputs followed the same approach as described earlier.

3. Results

3.1. Landslide Detection Accuracies

Figure 6 presents ML-LaDeCORsat performance results for validation sampling points at each case study site using CART, RF, GTB, or SVM classifier. In each case, S2-L1C (TOA) bands have been used as they resulted in slightly better detection accuracies compared to using SIAC-derived S2-L2A (SR) bands. Nevertheless, the shared ML-LaDeCORsat GEE scripts do include both options. The classification performance measures include TA, VA, Kappa, Spec, and Recall. BA and F1S outputs were almost identical to OA, so was Prec to Spec. Supplementary Tables S1 and S2 list the specific performance measures for these and all other validation metrics, as described in Section 2.2.5, for validation samples and for "all pixels" applying each of all available classifiers including NB.

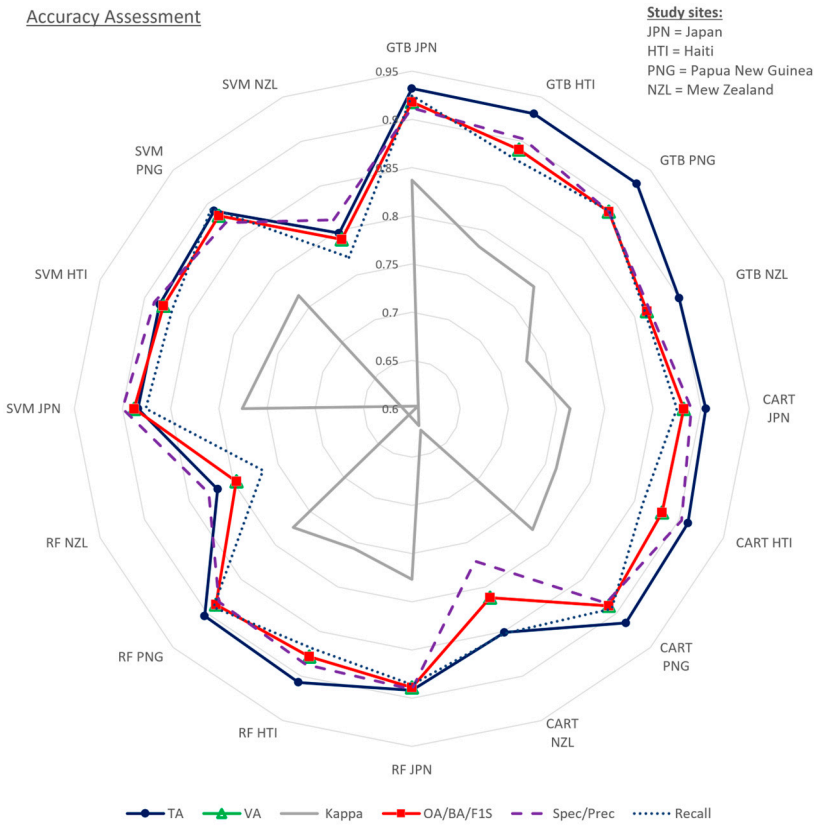

Figure 6. Comparison of accuracy assessments for ML-LaDeCORsat using various GEE ML classifiers: Classification and Regression Trees (GTB), Gradient Tree Boost (GTB), CART, Random Forest (RF), and Scalable Vector Machine (SVM).

Results clearly revealed that the GTB classifier achieved the best landslide detection accuracy with OA of 92% of all validation pixels correctly classified for JPN, 89% for HTI and PNG, and 86% for NZL. CART, RF, and SVM classifiers performed less accurately resulting in an OA of 80–88%. Using NB did result in the least accurate prediction of only 49–57%. Comparing different classifiers based on the amount of overfitting (differences between training and validation accuracy), all classifiers indicate very small differences of less than 4%, indicating that the model is not overfitted.

To compare the best detection accuracy achieved using ML-LaDeCORsat with GTB, landslides of all four case studies were predicted in GEE using one or more bands that represent existing methods or additional landslide condition bands as previously presented in Table 1. The resulting "all pixel"-based BA and Kappa validation values are listed in Figure 7. In each case, ML-LaDeCORsat outperformed all existing methods. The work of [44] utilizing a supervised classification applied to four conditioning factors (NDWIpost, NDVIpost, DEM, and slope) was identified as the best-performing existing method, but it achieved, taking the JPN case study as an example, 5% lower BA and 10% lower Kappa than ML-LaDeCORsat. Detailed accuracy assessment can be found in Supplementary Table S3 until Table S6. Running ML-LaDeCORsat with the best-performing classifier, GTB, a binary classified landslide map was created as well as an error map (Figure 8) providing visual insights into the distribution and spatial density of TN and FN within the study area.

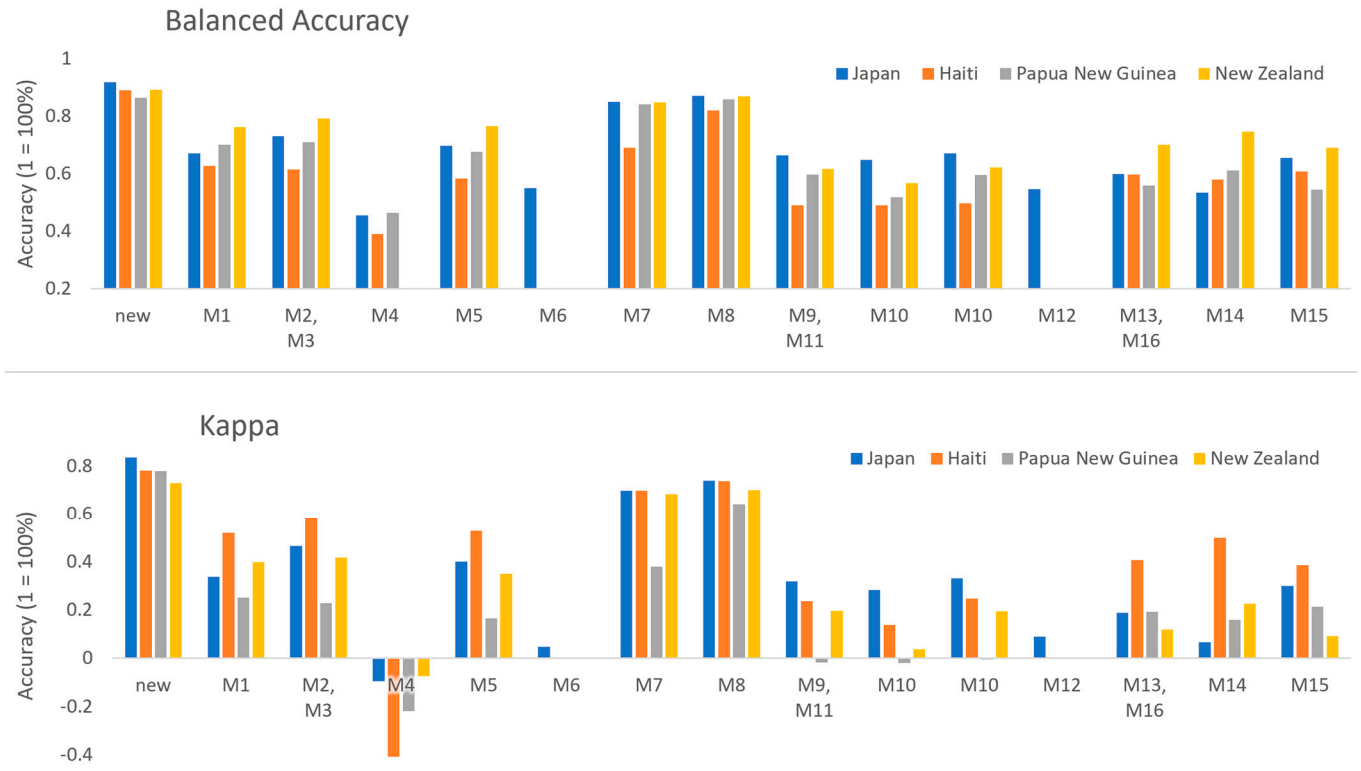

Figure 7. Comparison of GTB-based ML-LaDeCORsat (new) with existing landslide detection methods (M1–M15 as listed in Table 1) applied to all 4 case studies using balanced accuracy (**top**) and kappa (**bottom**) as performance indicators. M6: Unsupervised classification for Haiti, Papua New Guinea, and New Zealand reached computational limits in GEE; M12: P2 bands not available for Haiti, Papua New Guinea, and New Zealand.

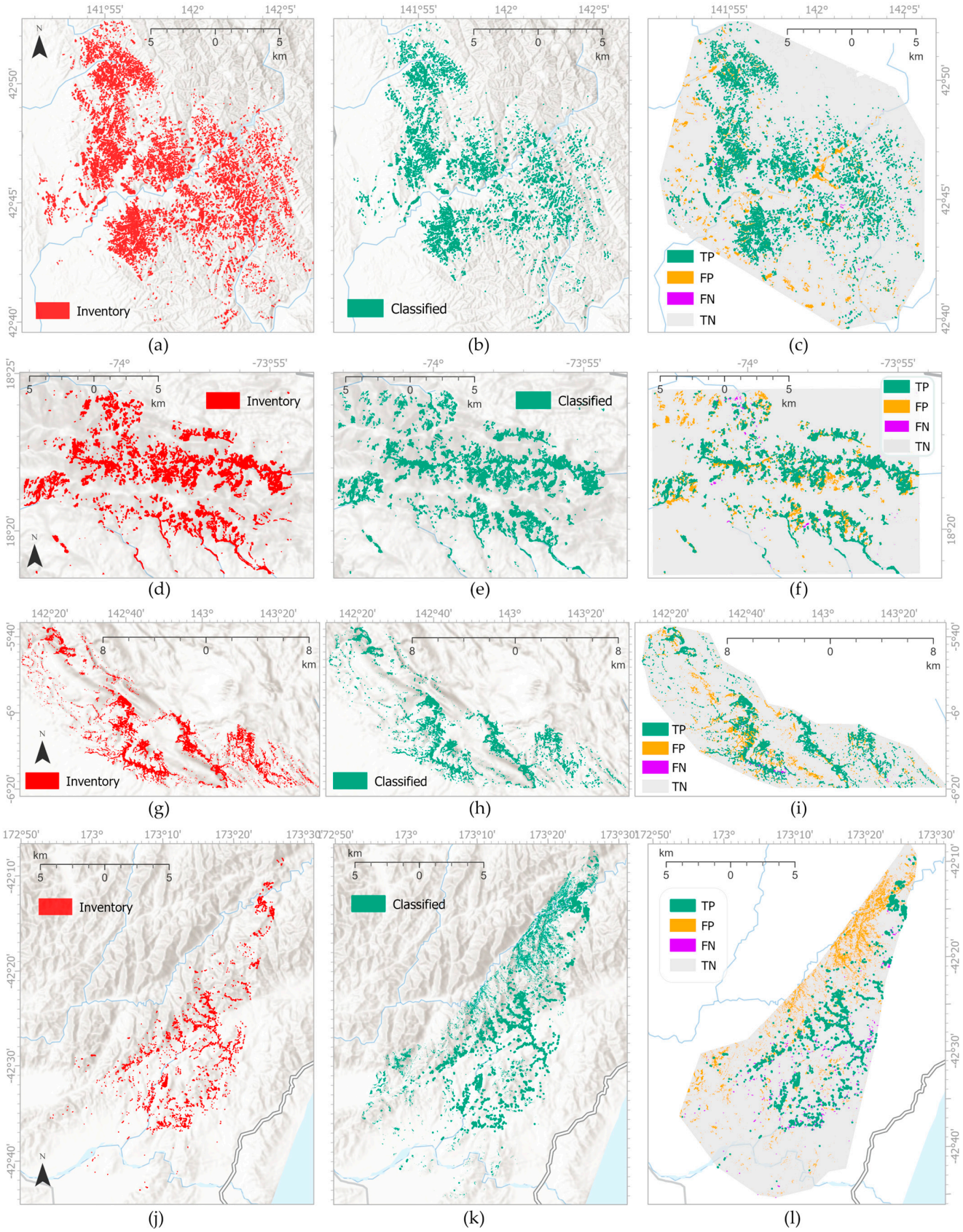

Figure 8. Landslide inventories, predicted landslides using ML-LaDeCORsat with the best-performing classifier, and error maps for Japan (**a**–**c**), Haiti (**d**–**f**), Papua New Guinea (**g**–**i**), and New Zealand (**j**–**l**).

3.2. Importance Factors of Landslide Conditioning Bands

For investigating the importance of each landslide conditioning band for ML-LaDeCORsat accuracy, we used band importance values provided as an output of the GEE *classifier.explain()* function, which is available for CART, RF, and GTB. Figure 9 displays normalized GEE band importance values for each of these three classifiers. High values indicate high-importance factors. For all three classifiers, the following bands showed the highest importance factors: $NDVI_{post}$, BSI_{post}, dem, S1_log_VH, ΔB4, ΔB5, ΔNDWI. Surprisingly, S2 NIR and SWIR bands were less important. Further experiments investigating the detection performance with or without S1 bands confirmed for each case study that including S1-derived bands always improved landslide detection accuracy. It should be noted that the P2_log_HV band is not included in Figure 9 since it was only used for the JPN case study. It had average importance for GTB (normalized importance of 0.2) and for CART (0.12), and no importance for the RF classifier (0.05).

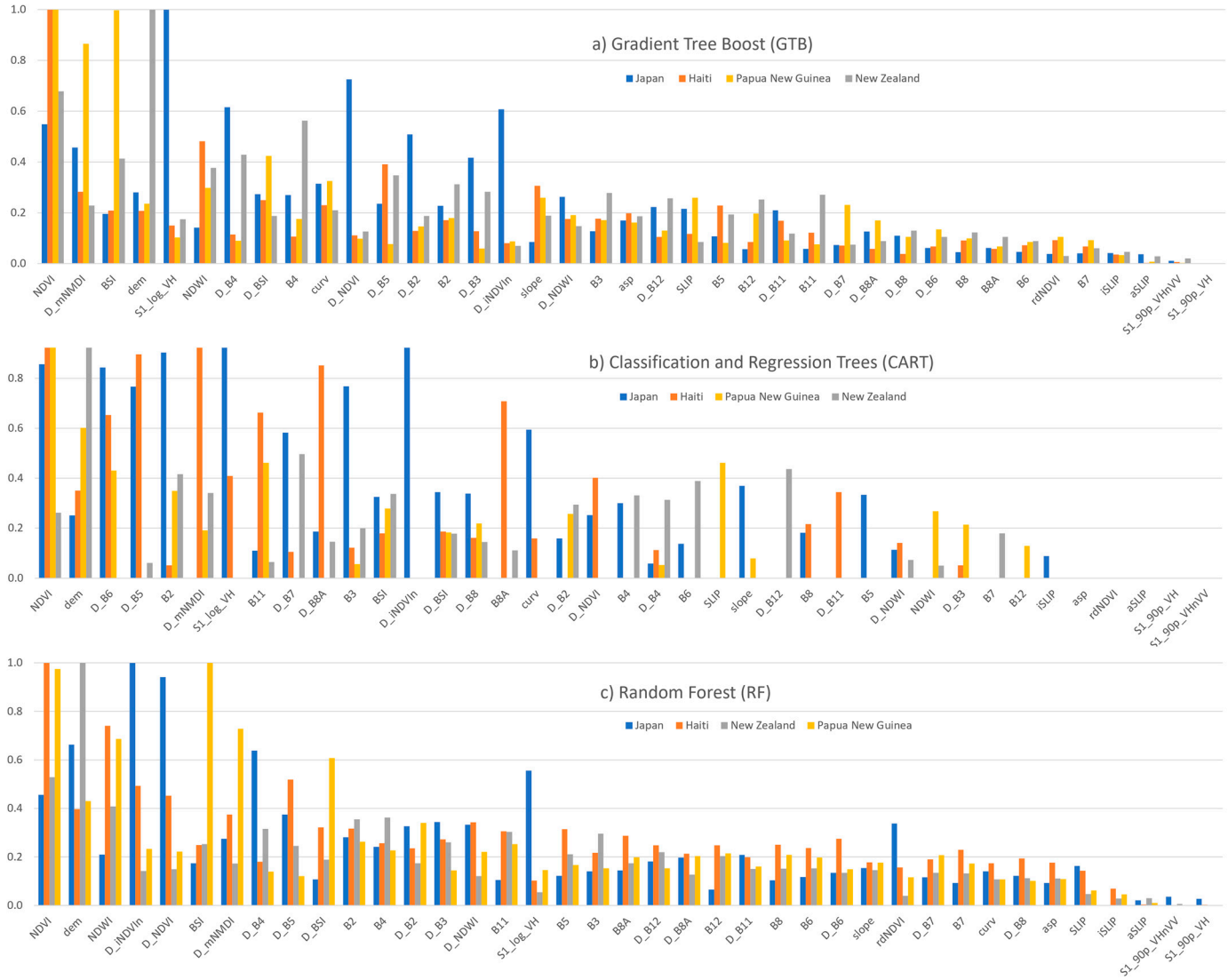

Figure 9. Importance of various landslide conditioning bands for ML-LaDeCORsat accuracy based on normalized sorted band importance for each study site using either (**a**) GTB, (**b**) CART, and (**c**) RF. Classifiers are sorted by their sum over all case studies and high values indicate high-importance factors.

Using the JPN case study, Table 6 lists OA and BA as well as Earth Engine Compute Unit (EECU) in minutes, representing the amount of instantaneous processing power, peak memory (MB), and the count of operations for running the entire GEE script including

image compilation, filtering, calculation of pseudobands, image band stacking, training the ML classifier, etc. OA, BA, and the three computational measures are provided for running the script with all 40 bands for all classifiers and with using only the best 20, 15, 10, or 5 bands for the three best-performing classifiers, GTB, RF, and CART. Results clearly indicate the benefit of using a selected number of identified important bands in an ML classifier for the used processing power in GEE. Using a significantly reduced number of bands, identified as the most important, still allows for the detection of landslides with an OA of 89%, and it also significantly reduces computation efforts in GEE. Computational savings revealed time savings of up to 87%, peak memory reduction of up to 72%, and a decrease in used operations of up to 23%. The computational time for our ML-LaDeCORsat scripts when applied to other landslide case study areas will depend mainly on the size of the study area. Detailed accuracy assessment for running ML-LaDeCORsat with selected important bands can be found in Supplementary Tables S7–S9.

Table 6. Measures of computational load of ML classifiers in GEE using all 39 or 20/15/10/5 selected most important bands for the Japan case study.

Used Bands	Classifier	Validation Pixels		All Pixels		EECU Minutes [1]		Peak Memory (MB) [1]		Count of Operations [1]	
		OA	BA	OA	BA						
All 40 bands	CART	0.883	0.869	0.883	0.869	3.1		19,515,864		2490	
	RF	0.889	0.876	0.889	0.876	37.9		23,429,664		2490	
	GTB	0.919	0.894	0.919	0.894	47.1		26,217,076		2490	
	SVM	0.888	0.871	0.888	0.871	53.6		62,084,948		1834	
	NB	0.668	0.607	0.668	0.607	2.7		19,359,664		1830	
20 most important bands	CART	0.881	0.866	0.881	0.866	2.4	24%	9,168,112	53%	2068	17%
	RF	0.891	0.875	0.891	0.875	20.0	47%	15,366,896	34%	2068	17%
	GTB	0.917	0.894	0.917	0.894	17.6	63%	17,570,796	33%	2088	16%
15 most important bands	CART	0.881	0.872	0.881	0.872	2.2	29%	7,940,596	59%	2018	19%
	RF	0.891	0.875	0.891	0.875	12.8	66%	14,440,848	38%	2018	19%
	GTB	0.913	0.892	0.913	0.892	13.2	72%	16,044,596	39%	2018	19%
10 most important bands	CART	0.881	0.875	0.881	0.875	2.1	32%	6,713,312	66%	1968	21%
	RF	0.885	0.874	0.885	0.874	14.6	61%	13,510,296	42%	1968	21%
	GTB	0.910	0.890	0.910	0.89	9.5	80%	15,033,080	43%	1968	21%
5 most important bands [2]	CART	0.868	0.865	0.868	0.865	2.0	36%	5,402,080	72%	1918	23%
	GTB	0.890	0.881	0.890	0.881	6.3	87%	14,090,680	46%	1918	23%

[1] and resulting percentual computational savings compared to using all 40 bands. [2] not available for RF due to minimum of 10 nodes requirement.

If our shared scripts are applied to other landslide case study areas, computational measures will depend mainly on the size of the study area.

3.3. Transfer Learning

Results for across-domain transfer learning investigations using the best-performing classifier (GTB) for ML-LaDeCORsat are presented in Figure 10.

For each case study site, OA, BA, and Recall metrics are plotted against different training options: using all training samples from (1) the target site, (2) all other sites, (3) the "best performing" other sites, 4–10) the "best performing" other sites plus a subset (50/40/30/20/10/5/1%) of the target site. The "best performing" other sites have been identified by comparing detection accuracies for a target site using all possible combinations of across-domain training sites (e.g., training option for JPN target site: HTI only; PNG

only; NZL only; HTI and PNG; PNG and NZL; HTI and NZL; all three). Consequently, HTI and PNG combined resulted in the best-performing training sites for target JPN. JPN and PNG combined resulted in the best-performing training sites for target HTI. The best results for PNG delivered the GTB classifier trained by only JPN. For NZL, all other three sites combined resulted as the best option. Detailed accuracy assessment for across site transfer learning can be found in Supplementary Tables S10–S13.

Figure 10. Across sites transfer learning and accuracies using the best-performing classifier (GTB) for ML-LaDeCORsat and "all pixel" validation. OA, BA, and recall metrics of accuracy are plotted against different training options: using all training samples from the target site (first position in each graph), all sites (second), all other sites without target site (third), and the "best performing" other sites plus a subset (50/40/30/20/10/5/1%) of the target site (all other positions). The "best performing" other sites have been identified by comparing detection accuracies for a target site using all possible combinations of across-domain training sites (e.g., training option for JPN target site: HTI only; PNG only; NZL only; HTI and PNG; PNG and NZL; HTI and NZL; all three).

4. Discussion and Conclusions

We propose a novel machine learning-based approach for Coseismic Landslide Detection using Combined Optical and Radar Satellite Imagery (ML-LaDeCORsat), to identify the locations of landslides using freely available imagery in GEE. Furthermore, we demonstrate the improved reliability and accuracy of the approach by comparing its performance with other methods using a landslide event triggered by four different earthquake case studies. ML-LaDeCORsat is an automated approach that is freely available on GEE. The required training data is also available and, therefore, does not have to be created by the user. These script and training data facilitate fast (6.3–47.1 EECU minutes for GTB) and reliable (0.890–0.919 OA for GTB) identification of coseismic landslides as part of disaster management on a global scale.

Given that the main purpose of rapidly identifying landslides is to improve disaster management responses, accuracy is a key criterion for any approach. The prediction accuracy is impacted by several aspects, including ML sampling design (number of sampling points, distribution and density, topographic and other factors to be considered in a stratified sampling approach), spatial accuracy and precision of geo-referenced landslide inventory polygons, used satellite imagery and derived pseudobands, image processing steps, the used ML classifier, its parameters, and the chosen evaluation metrics. In this study, all these aspects were carefully investigated and addressed to achieve the best possible landslide detection accuracy in GEE while using ready-made datasets in GEE. Comparisons with existing approaches [19,29,31–34,38–42,44–48] demonstrated superior performance of ML-LaDeCORsat of at least 10% higher detection accuracy.

Compared to previous RS-based landslide detection research, this study has, to our knowledge for the first time in literature, combined various relevant landslide conditioning bands utilizing S2 spectral reflectance bands and indices with radar-derived backscatter change information into a single feature matrix used to train a ML model. Furthermore, the performance of the ML-LaDeCORsat model has been tested by applying different available GEE ML classifiers and compared to existing solutions incorporating all validation sampling points, but then also using all pixels to have the best possible accuracy assessment. The GTB ML classifier revealed the best prediction results, for all study sites with OA of 92% compared to CART with 88%, RF with 89%, SVM with 89%, and NB with 66% validation pixels correctly classified, taking the JPN case study as an example.

A landslide-specific sampling design combined with a novel slope- and slope-buffer-based masking approach was demonstrated to be highly effective in reducing FP, in particular in scenarios where a landslide flow area reached pixels with slopes below the slope threshold. In addition, applying a Gaussian kernel filter to the predicted landslide map helped to remove isolated single FP pixels. All four case study sites included a large variation of sparse to densely vegetated areas, suggesting that the proposed landslide detection solution performs well across different vegetation cover.

In summary, the introduced novel ML-LaDeCORsat approach significantly improves landslide detection through image combining optical and radar imagery and ML and is easily adaptable to other landslide scenarios with the GEE script being available.

Pixel size, source data accuracy, and imagery availability on GEE pose limitations on ML-LaDeCORsat that could be partially addressed in future studies. In case a sampling pixel is located at the edge of a landslide, it is either defined as a landslide pixel or as a non-landslide one, depending on whether the respective part of a landslide inventory polygon covers more (or less) than 50% of an image pixel. Smaller imagery pixel size and more accurate landslide inventory boundaries will lower the potential occurrences of such false sampling cases and, consequently, improve detection accuracies. Sampling pixels located on landslide inventory edges could also be removed or avoided. In regard to the quality of the landslide inventory dataset used, it was discovered that at a few locations, in particular at the edge of some landslide polygons, the inventory did not always match with the visual landslide information available from a very high (sub-meter) resolution true-color satellite composite (accessed through Google Earth Pro). A manual correction of

these mismatches could potentially further improve prediction accuracies. A few of the randomly distributed training and validation samples were positioned over pixels located near the edge of a landslide inventory polygon, causing the use of a potential false sample. Although an undertaken verification of sampling points did not reveal any false samples, it was not possible to manually inspect all of them due to the large amount of sampling points (60,000 for each study site). Detection results could be further improved by incorporating each of the following additional bands—if made available in GEE at a reasonably high spatial resolution (e.g., of 20 m or better): TWI, STI, geological structure, and soil moisture data from advanced SAR processing [80], or a raster image with annual rainfall data. This study also lacked post-earthquake elevation data, but if available, the inclusion of data containing precise elevation changes could potentially further enhance the accuracy of the detection results. Although transfer learning investigations confirmed the model's general applicability of ML-LaDeCORsat, strategies for source and target domain selection, and specific impacts on landslide classification performance could be further explored [81]. Lastly, the availability of post-earthquake S1 imagery and near cloud-free S2 imagery does impact timely landslide detection when using our approach.

There are plans to extend this work. Firstly, we hope to further improve detection results by considering the pixel neighborhoods within the ML classification—similar to [38] and by including additional imagery that is not available in GEE, that is PlanetScope (Dove/SuperDove) or VHR historical RGB Satellite Imagery extracted from GE [82]. Secondly, we plan to convert our GEE JavaScript solution into a GEE Python Notebook to access TensorFlow libraries for further advancing the ML model. Thirdly, our approach could be tested with different landslide types, such as avalanche or mudslide where optical and radar input imagery likely comprises different spectral characteristics. It may be particularly important to apply the approach to landslide events triggered by extreme weather events, such as heavy rainfall, which are forecast to become more frequent or more intense under anthropogenic climate change [83]. For example, the rainfall associated with tropical cyclones (also known as hurricanes or typhoons) is known to trigger landslide events and is forecast to increase in intensity [84–86]. Depending on data availability, further research may provide insights into how factors such as soil moisture and geological structure can affect the model's generalizability. Lastly, the suggested ML-LaDeCORsat approach could be adapted to improve existing work on landslide susceptibility [11–13]. Accurate and rapid identification of landslides will likely become more important because extreme weather events are forecast to become more frequent, implying an increased likelihood of earthquakes following heavy precipitation events, which would increase the number of associated landslides.

Supplementary Materials: The following supporting information can be downloaded at: https://www.mdpi.com/article/10.3390/rs16101722/s1, Table S1. Accuracy assessment for ML-LaDeCORsat applied to JPN and HTI study sites. Table S2. Accuracy assessment for ML-LaDeCORsat applied to PNG and NZL study sites. Table S3. Accuracy Assessment of existing landslide detection methods for JPN case study. Table S4. Accuracy Assessment of existing landslide detection methods for HTI case study. Table S5. Accuracy Assessment of existing landslide detection methods for PNG case study. Table S6. Accuracy Assessment of existing landslide detection methods for NZL case study. Table S7. Normalized sorted band importance outputs for ML-LaDeCORsat for each study site using GTB, CART, or RF ML classifier, sorted by their overall sum. Table S8. Accuracy Assessment for ML-LaDeCORsat using selected bands—case study JPN. Table S9. Accuracy Assessment for ML-LaDeCORsat using selected bands—case study HTI. Table S10. Accuracy Assessment for ML-LaDeCORsat using Transfer Learning for JPN. Table S11. Accuracy Assessment for ML-LaDeCORsat using Transfer Learning for HTI. Table S12. Accuracy Assessment for ML-LaDeCORsat using Transfer Learning for PNG. Table S13. Accuracy Assessment for ML-LaDeCORsat using Transfer Learning for NZL. Table S14. Temporal filtering of utilized S2, S1, P2 imagery.

Author Contributions: Conceptualization, S.P., P.X. and J.L.; Methodology, S.P., G.K. and A.W.; Software, S.P.; Validation, S.P. and J.L.; Formal Analysis, S.P.; Investigation, S.P.; Resources, S.P.; Data Curation, S.P.; Writing—Original Draft Preparation, S.P.; Writing—Review & Editing, J.L., G.K., A.W.

and P.X.; Visualization, S.P.; Project Administration, S.P.; Funding Acquisition, S.P. All authors have read and agreed to the published version of the manuscript.

Funding: The University of South Australia, Unit of Science, Technology, Engineering and Mathematics (STEM) supported this project financially through the Professional Experience Program 2023, Ref 230314-001821, granted to the first author.

Data Availability Statement: Publicly available Google Earth Engine (GEE) scripts and datasets develop and used in this study can be found in the following GEE repository: https://code.earthengine.google.com/?accept_repo=users/speterstum/ML_LaDeCORSat (accessed on 1 May 2024). The GEE repository includes scripts with our implemented ML-LaDeCORsat landslide detection method, and scripts of previously existing landslide detection methods (for comparison) implemented and validated in GEE using inventory dataset for four case studies. The GEE repository includes the following scripts: [(1) *LaDeCORsat_JPN*: Japan, Hokkaido, Iburi 2018 case study; (2) *LaDeCORsat_HTI*: Haiti, Tiburon Peninsula, Pic Macaya NP 2021 case study; (3) *LaDeCORsat_PNG*: Papua New Guinea, Hela Province, Komo, 2018 case study; (4) *LaDeCORsat_NZL*: New Zealand, Kaikōura 2016 case study; (5) *LaDeCORsat_Transfer_Learning*: across study sites training and classification; (6) *Other_landslides_detection_methods*: implemented landslide detection methods as presented in Table 1 and Figure 7.] These GEE scripts include shared GEE assets. For each case study shared assets include a study area polygon ("AOI"), landslide ground truthing polygons ("GT"), a pre-processed multi-band stacked input image ("img_for_ML") and training and validation point samples. The satellite imagery data used in this paper were provided by the ESA Copernicus program and by NASA and accessed through GEE (https://code.earthengine.google.com, accessed on 1 May 2024).

Acknowledgments: We would like to thank the ESA Copernicus program, NASA, and GEE for providing freely available satellite imagery data and cloud-based processing tools. We also acknowledge Zhang, Li, Wang and Iio [35] for providing the Hokkaido landslide inventory. Part of this research was carried out at Kyoto University, Disaster Prevention Research Institute (DPRI), which we thank for cooperation in the form of hosting the first author as a Visiting Research Fellow.

Conflicts of Interest: The authors declare no conflicts of interest.

Abbreviations

The following abbreviations are used in this paper:

AOI	Area of interest
BA	Balanced Accuracy
BSI	Bare Soil Index
CART	Classification and Regression Trees
CE	Commission Error
CNN	Convolutional Neural Network
DL	Deep Learning
EECU	Earth Engine Compute Unit
ESA	European Space Agency
FN	False Negative
FP	False Positive
gDEM	Global Digital Elevation Model
GE	Google Earth
GEE	Google Earth Engine
GTB	Gradient Tree Boost
IR	Infra-Red
iSLIP	Improved Sudden Landslide Identification Product
L8	Landsat-8
LULC	Land Use Land Cover
ML	Machine learning
MODIS	Moderate Resolution Imaging Spectroradiometer
N_{area}	Area for negative training samples
N-B_{area}	Area for negative training samples inside ring-buffers
NASA	National Aeronautics and Space Administration
NB	Naive Bayes

NDVI	Normalized Difference Vegetation Index
NIR	Near-Infra-Red
NRT	Near real-time
OA	Overall accuracy
OE	Omission error
PCA	Principal component analysis
P2	Palsar-2
QP	Quality percentage
RF	Random Forest
RS	Remote Sensing
S1	Sentinel-1
S2	Sentinel-2
SIAC	Sensor Invariant Atmospheric Correction
SLIP	Sudden Landslide Identification Product
SR	Surface reflectance
STI	Sediment Transport Index
SVM	Scalable Vector Machine
SWIR	Short-Wave Infra-Red
TA	Training accuracy
TN	True Negative
TOA	Top-Of-Atmosphere (reflectance)
TOA2SR	Top of Atmosphere reflectance corrected to Surface Reflectance
P_{area}	Area for positive training samples (ground truth)
TP	True positive
TWI	Topographic Wetness Index
VA	Validation Accuracy
VHR	Very high-resolution

References

1. Highland, L.; Bobrowsky, P.T. *The Landslide Handbook: A Guide to Understanding Landslides*; US Geological Survey: Reston, VA, USA, 2008.
2. Keefer, D.K. Landslides Caused by Earthquakes. *Geol. Soc. Am. Bull.* **1984**, *95*, 406–421. [CrossRef]
3. Ritchie, H.; Roser, M. Natural Disasters. Available online: https://ourworldindata.org/natural-disasters (accessed on 9 July 2023).
4. Wallemacq, P.; Below, R.; McClean, D. Economic Losses, Poverty & Disasters: 1998–2017. United Nations Office for Disaster Risk Reduction. 2018. Available online: https://www.preventionweb.net/files/61119_credeconomiclosses.pdf (accessed on 17 September 2023).
5. Quigley, M.; Duffy, B. Effects of Earthquakes on Flood Hazards: A Case Study from Christchurch, New Zealand. *Geosciences* **2020**, *10*, 114. [CrossRef]
6. Noy, I.; Okubo, T.; Strobl, E.; Tveit, T. The Fiscal Costs of Earthquakes in Japan. *Int. Tax Public Financ.* **2022**, *30*, 1225–1250. [CrossRef]
7. Cruden, D.M. Cruden, Dm, Varnes, Dj, 1996, Landslide Types and Processes, Transportation Research Board, Us National Academy of Sciences, Special Report, 247: 36–75. *Landslides Eng. Pract.* **1993**, *24*, 20–47.
8. Stanley, T.A.; Kirschbaum, D.B.; Benz, G.; Emberson, R.A.; Amatya, P.M.; Medwedeff, W.; Clark, M.K. Data-Driven Landslide Nowcasting at the Global Scale. *Front. Earth Sci.* **2021**, *9*, 640043. [CrossRef]
9. Ruggeri, P.; Fruzzetti, V.M.; Ferretti, A.; Scarpelli, G. Seismic and Rainfall Induced Displacements of an Existing Landslide: Findings from the Continuous Monitoring. *Geosciences* **2020**, *10*, 90. [CrossRef]
10. Saito, H.; Uchiyama, S.; Hayakawa, Y.S.; Obanawa, H. Landslides Triggered by an Earthquake and Heavy Rainfalls at Aso Volcano, Japan, Detected by Uas and Sfm-Mvs Photogrammetry. *Prog. Earth Planet. Sci.* **2018**, *5*, 15. [CrossRef]
11. Zhao, Y.; Huang, Z.; Wei, Z.; Zheng, J.; Konagai, K. Assessment of Earthquake-Triggered Landslide Susceptibility Considering Coseismic Ground Deformation. *Front. Earth Sci.* **2023**, *10*, 993975. [CrossRef]
12. Ali, S.A.; Parvin, F.; Vojteková, J.; Costache, R.; Linh, N.T.T.; Pham, Q.B.; Vojtek, M.; Gigović, L.; Ahmad, A.; Ghorbani, M.A. GIS-Based Landslide Susceptibility Modeling: A Comparison between Fuzzy Multi-Criteria and Machine Learning Algorithms. *Geosci. Front.* **2021**, *12*, 857–876. [CrossRef]
13. Fan, X.; Liu, B.; Luo, J.; Pan, K.; Han, S.; Zhou, Z. Comparison of Earthquake-Induced Shallow Landslide Susceptibility Assessment Based on Two-Category LR and KDE-MLR. *Sci. Rep.* **2023**, *13*, 833. [CrossRef]
14. Dell'Acqua, F.; Gamba, P. Remote Sensing and Earthquake Damage Assessment: Experiences, Limits, and Perspectives. *Proc. IEEE* **2012**, *100*, 2876–2890. [CrossRef]

15. Yao, T.; Green, D.; Michael, K.; Davies, D. Using Nasa Lance near Real-Time Products for Disaster Risk Reduction. In Proceedings of the FOSS4G 2021 (Free and Open Source Software for Geospatial), Online, 27 September–2 October 2021.
16. NASA. Near Real Time (Nrt) Data from Esa Sentinel Satellites. 2021. Available online: https://appliedsciences.nasa.gov/join-mission/publications-resources/near-real-time-nrt-data-esa-sentinel-satellites (accessed on 21 September 2023).
17. Shafapourtehrany, M.; Batur, M.; Shabani, F.; Pradhan, B.; Kalantar, B.; Özener, H. A Comprehensive Review of Geospatial Technology Applications in Earthquake Preparedness, Emergency Management, and Damage Assessment. *Remote Sens.* **2023**, *15*, 1939. [CrossRef]
18. Liu, X.; Zhao, C.; Zhang, Q.; Lu, Z.; Li, Z.; Yang, C.; Zhu, W.; Liu-Zeng, J.; Chen, L.; Liu, C. Integration of Sentinel-1 and Alos/Palsar-2 Sar Datasets for Mapping Active Landslides Along the Jinsha River Corridor, China. *Eng. Geol.* **2021**, *284*, 106033. [CrossRef]
19. Handwerger, A.L.; Huang, M.-H.; Jones, S.Y.; Amatya, P.; Kerner, H.R.; Kirschbaum, D.B. Generating Landslide Density Heatmaps for Rapid Detection Using Open-Access Satellite Radar Data in Google Earth Engine. *Nat. Hazards Earth Syst. Sci.* **2022**, *22*, 753–773. [CrossRef]
20. Wang, W.; Motagh, M.; Plank, S.; Orynbaikyzy, A.; Roessner, S. Application of Sar Time-Series and Deep Learning for Estimating Landslide Occurrence Time. *Int. Arch. Photogramm. Remote Sens. Spat. Inf. Sci.* **2022**, *43*, 1181–1187. [CrossRef]
21. Jensen, J.R. *Remote Sensing of the Environment: An Earth Resource Perspective 2/E*; Pearson Education: Noida, India, 2009.
22. Fitzgerald, D.L.; Peters, S.; Guerin, G.R.; McGrath, A.; Keppel, G. Quantifying Dieback in a Vulnerable Population of Eucalyptus Macrorhyncha Using Remote Sensing. *Land* **2023**, *12*, 1271. [CrossRef]
23. Schmitt, M.; Hughes, L.H.; Qiu, C.; Zhu, X.X. Aggregating Cloud-Free Sentinel-2 Images with Google Earth Engine. *ISPRS Ann. Photogramm. Remote Sens. Spat. Inf. Sci.* **2019**, *4*, 145–152.
24. Martinez, S.N.; Schaefer, L.N.; Allstadt, K.E.; Thompson, E.M. Evaluation of Remote Mapping Techniques for Earthquake-Triggered Landslide Inventories in an Urban Subarctic Environment: A Case Study of the 2018 Anchorage, Alaska Earthquake. *Front. Earth Sci.* **2021**, *9*, 673137. [CrossRef]
25. Ray, R.L.; Lazzari, M.; Olutimehin, T. Remote Sensing Approaches and Related Techniques to Map and Study Landslides. *Landslides-Investig. Monit* **2020**, *2*, 1–25.
26. Xu, C.; Gorum, T.; Tanyas, H. Application of Remote Sensing and Gis in Earthquake-Triggered Landslides. *Front. Earth Sci.* **2022**, *10*, 964753. [CrossRef]
27. Byrraju, S.V. *Landslide Detection Using Remote Sensing Methods A Review of Current Techniques*; University of South Carolina: Columbia, SC, USA, 2019.
28. Kader, M.A.; Jahan, I. A Review of the Application of Remote Sensing Technologies in Earthquake Disaster Management: Potentialities and Challenges. In Proceedings of the International Conference on Disaster Risk Management, Dhaka, Bangladesh, 12–14 January 2019; pp. 12–14.
29. Notti, D.; Cignetti, M.; Godone, D.; Giordan, D. Semi-Automatic Mapping of Shallow Landslides Using Free Sentinel-2 and Google Earth Engine. *Nat. Hazards Earth Syst. Sci. Discuss.* **2023**, *23*, 2625–2648. [CrossRef]
30. Lu, P.; Qin, Y.; Li, Z.; Mondini, A.C.; Casagli, N. Landslide Mapping from Multi-Sensor Data through Improved Change Detection-Based Markov Random Field. *Remote Sens. Environ.* **2019**, *231*, 111235. [CrossRef]
31. Shahabi, H.; Rahimzad, M.; Tavakkoli Piralilou, S.; Ghorbanzadeh, O.; Homayouni, S.; Blaschke, T.; Lim, S.; Ghamisi, P. Unsupervised Deep Learning for Landslide Detection from Multispectral Sentinel-2 Imagery. *Remote Sens.* **2021**, *13*, 4698. [CrossRef]
32. Fayne, J.V.; Ahamed, A.; Roberts-Pierel, J.; Rumsey, A.C.; Kirschbaum, D. Automated Satellite-Based Landslide Identification Product for Nepal. *Earth Interact.* **2019**, *23*, 1–21. [CrossRef]
33. Ngandam Mfondoum, A.H.; Wokwenmendam Nguet, P.; Mefire Mfondoum, J.V.; Tchindjang, M.; Hakdaoui, S.; Cooper, R.; Gbetkom, P.G.; Penaye, J.; Bekoa, A.; Moudioh, C. Adapting Sudden Landslide Identification Product (SLIP) and Detecting Real-Time Increased Precipitation (DRIP) Algorithms to Map Rainfall-Triggered Landslides in Western Cameroon Highlands (Central-Africa). *Geoenviron. Disasters* **2021**, *8*, 17. [CrossRef]
34. Piralilou, S.T.; Shahabi, H.; Pazur, R. Automatic Landslide Detection Using Bi-Temporal Sentinel 2 Imagery. *GI_Forum* **2021**, *9*, 39–45. [CrossRef]
35. Zhang, S.; Li, R.; Wang, F.; Iio, A. Characteristics of Landslides Triggered by the 2018 Hokkaido Eastern Iburi Earthquake, Northern Japan. *Landslides* **2019**, *16*, 1691–1708. [CrossRef]
36. Sivasankar, T.; Ghosh, S.; Joshi, M. Exploitation of Optical and SAR Amplitude Imagery for Landslide Identification: A Case Study from Sikkim, Northeast India. *Environ. Monit. Assess.* **2021**, *193*, 386. [CrossRef] [PubMed]
37. Yang, W.; Qi, W.; Fang, J. Using Google Earth Engine to Monitor Co-Seismic Landslide Recovery after the 2008 Wenchuan Earthquake. *Earth Surf. Dyn. Discuss.* **2020**, *2020*, 1–14.
38. Ghorbanzadeh, O.; Shahabi, H.; Crivellari, A.; Homayouni, S.; Blaschke, T.; Ghamisi, P. Landslide Detection Using Deep Learning and Object-Based Image Analysis. *Landslides* **2022**, *19*, 929–939. [CrossRef]
39. Aimaiti, Y.; Liu, W.; Yamazaki, F.; Maruyama, Y. Earthquake-Induced Landslide Mapping for the 2018 Hokkaido Eastern Iburi Earthquake Using PALSAR-2 data. *Remote Sens.* **2019**, *11*, 2351. [CrossRef]
40. Ariza, A.; Davila, N.A.; Kemper, H.; Kemper, G. Landslide Detection in Central America Using the Differential Bare Soil Index. *Int. Arch. Photogramm. Remote Sens. Spat. Inf. Sci.* **2021**, *43*, 679–684. [CrossRef]

41. Yu, B.; Chen, F.; Muhammad, S. Analysis of Satellite-Derived Landslide at Central Nepal from 2011 to 2016. *Environ. Earth Sci.* **2018**, *77*, 331. [CrossRef]
42. Subiyantoro, A.; Westen, C.J.V.; Bout, B.V.D.; Yuniawan, R.A.; Mulyana, A.R. Semi-automatic Landslide Detection Using Google Earth Engine, a Case Study in Poi Village, Central Sulawesi. In Proceedings of the 2022 IEEE International Conference on Aerospace Electronics and Remote Sensing Technology (ICARES), Yogyakarta, Indonesia, 24–25 November 2022; pp. 1–4.
43. Scheip, C.M.; Wegmann, K.W. HazMapper: A Global Open-Source Natural Hazard Mapping Application in Google Earth Engine. *Nat. Hazards Earth Syst. Sci.* **2021**, *21*, 1495–1511. [CrossRef]
44. Singh, P.; Maurya, V.; Dwivedi, R. Pixel Based Landslide Identification Using Landsat 8 and Gee. In Proceedings of the 2021 IEEE International Geoscience and Remote Sensing Symposium IGARSS, Brussels, Belgium, 11–16 July 2021; pp. 8444–8447.
45. Lindsay, E.; Frauenfelder, R.; Rüther, D.; Nava, L.; Rubensdotter, L.; Strout, J.; Nordal, S. Multi-Temporal Satellite Image Composites in Google Earth Engine for Improved Landslide Visibility: A Case Study of a Glacial Landscape. *Remote Sens.* **2022**, *14*, 2301. [CrossRef]
46. Handwerger, A.L.; Jones, S.Y.; Huang, M.-H.; Amatya, P.; Kerner, H.R.; Kirschbaum, D.B. Rapid Landslide Identification Using Synthetic Aperture Radar Amplitude Change Detection on the Google Earth Engine. *Nat. Hazards Earth Syst. Sci. Discuss.* **2020**, *2020*, 1–24.
47. Hernandez, N.D.; Pastrana, A.A.; Garcia, L.C.; de Leon, J.C.V.; Alvarez, A.Z.; Morales, L.D.; Nemiga, X.A.; Posadas, G.D. Co-Seismic Landslide Detection after M 7.4 Earthquake on June 23, 2020, in Oaxaca, Mexico, Based on Rapid Mapping Method Using High and Medium Resolution Synthetic Aperture Radar (Sar) Images. *Landslides* **2021**, *18*, 3833–3844. [CrossRef]
48. Fujiwara, S.; Nakano, T.; Morishita, Y.; Kobayashi, T.; Yarai, H.; Une, H.; Hayashi, K. Detection and Interpretation of Local Surface Deformation from the 2018 Hokkaido Eastern Iburi Earthquake Using Alos-2 Sar Data. *Earth Planets Space* **2019**, *71*, 64. [CrossRef]
49. Ju, Y.; Xu, Q.; Jin, S.; Li, W.; Su, Y.; Dong, X.; Guo, Q. Loess Landslide Detection Using Object Detection Algorithms in Northwest China. *Remote Sens.* **2022**, *14*, 1182. [CrossRef]
50. Yu, Z.; Chang, R.; Chen, Z. Automatic Detection Method for Loess Landslides Based on Gee and an Improved Yolox Algorithm. *Remote Sens.* **2022**, *14*, 4599. [CrossRef]
51. Zhao, L.; Liu, J.; Peters, S.; Li, J.; Oliver, S.; Mueller, N. Investigating the Impact of Using Ir Bands on Early Fire Smoke Detection from Landsat Imagery with a Lightweight Cnn Model. *Remote Sens.* **2022**, *14*, 3047. [CrossRef]
52. Gomes, V.C.; Queiroz, G.R.; Ferreira, K.R. An Overview of Platforms for Big Earth Observation Data Management and Analysis. *Remote Sens.* **2020**, *12*, 1253. [CrossRef]
53. Mutanga, O.; Kumar, L. Google Earth Engine Applications. *Remote. Sens.* **2019**, *11*, 591. [CrossRef]
54. Pérez-Cutillas, P.; Pérez-Navarro, A.; Conesa-García, C.; Zema, D.A.; Amado-Álvarez, J.P. What Is Going on within Google Earth Engine? A Systematic Review and Meta-Analysis. *Remote Sens. Appl. Soc. Environ.* **2023**, *29*, 100907. [CrossRef]
55. Smith, W.D.; Dunning, S.A.; Brough, S.; Ross, N.; Telling, J. Geraldine (Google Earth Engine Supraglacial Debris Input Detector): A New Tool for Identifying and Monitoring Supraglacial Landslide Inputs. *Earth Surf. Dyn.* **2020**, *8*, 1053–1065. [CrossRef]
56. Van Natijne, A.; Bogaard, T.; van Leijen, F.; Hanssen, R.; Lindenbergh, R. World-Wide Insar Sensitivity Index for Landslide Deformation Tracking. *Int. J. Appl. Earth Obs. Geoinf.* **2022**, *111*, 102829. [CrossRef]
57. Wu, W.; Zhang, Q.; Singh, V.P.; Wang, G.; Zhao, J.; Shen, Z.; Sun, S. A Data-Driven Model on Google Earth Engine for Landslide Susceptibility Assessment in the Hengduan Mountains, the Qinghai–Tibetan Plateau. *Remote Sens.* **2022**, *14*, 4662. [CrossRef]
58. Ilmy, H.F.; Darminto, M.R.; Widodo, A. Application of Machine Learning on Google Earth Engine to Produce Landslide Susceptibility Mapping (Case Study: Pacitan). In Proceedings of the IOP Conference Series: Earth and Environmental Science, Online, 26 August 2020; p. 012028.
59. Ado, M.; Amitab, K.; Maji, A.K.; Jasińska, E.; Gono, R.; Leonowicz, Z.; Jasiński, M. Landslide Susceptibility Mapping Using Machine Learning: A Literature Survey. *Remote Sens.* **2022**, *14*, 3029. [CrossRef]
60. Li, B.; Liu, K.; Wang, M.; He, Q.; Jiang, Z.; Zhu, W.; Qiao, N. Global Dynamic Rainfall-Induced Landslide Susceptibility Mapping Using Machine Learning. *Remote Sens.* **2022**, *14*, 5795. [CrossRef]
61. Khan, M.M.; Ghaffar, B.; Shahzad, R.; Khan, M.R.; Shah, M.; Amin, A.H.; Eldin, S.M.; Naqvi, N.A.; Ali, R. Atmospheric Anomalies Associated with the 2021 M W 7.2 Haiti Earthquake Using Machine Learning from Multiple Satellites. *Sustainability* **2022**, *14*, 14782. [CrossRef]
62. Wang, F.; Fan, X.; Yunus, A.P.; Siva Subramanian, S.; Alonso-Rodriguez, A.; Dai, L.; Xu, Q.; Huang, R. Coseismic Landslides Triggered by the 2018 Hokkaido, Japan (M W 6.6), Earthquake: Spatial Distribution, Controlling Factors, and Possible Failure Mechanism. *Landslides* **2019**, *16*, 1551–1566. [CrossRef]
63. Zhao, B.; Wang, Y.; Li, W.; Lu, H.; Li, Z. Evaluation of Factors Controlling the Spatial and Size Distributions of Landslides, 2021 Nippes Earthquake, Haiti. *Geomorphology* **2022**, *415*, 108419. [CrossRef]
64. Tanyaş, H.; Hill, K.; Mahoney, L.; Fadel, I.; Lombardo, L. The World's Second-Largest, Recorded Landslide Event: Lessons Learnt from the Landslides Triggered during and after the 2018 Mw 7.5 Papua New Guinea Earthquake. *Eng. Geol.* **2022**, *297*, 106504. [CrossRef]
65. Tanyaş, H.; Görüm, T.; Fadel, I.; Yıldırım, C.; Lombardo, L. An Open Dataset for Landslides Triggered by the 2016 Mw 7.8 Kaikōura Earthquake, New Zealand. *Landslides* **2022**, *19*, 1405–1420. [CrossRef]
66. Ohtani, M.; Imanishi, K. Seismic Potential around the 2018 Hokkaido Eastern Iburi Earthquake Assessed Considering the Viscoelastic Relaxation. *Earth Planets Space* **2019**, *71*, 57. [CrossRef]

67. Yamagishi, H.; Yamazaki, F. Landslides by the 2018 Hokkaido Iburi-Tobu Earthquake on September 6. *Landslides* **2018**, *15*, 2521–2524. [CrossRef]
68. Martinez, S.N.; Allstadt, K.E.; Slaughter, S.L.; Schmitt, R.G.; Collins, E.; Schaefer, L.N.; Ellison, S. *Landslides Triggered by the August 14, 2021, Magnitude 7.2 Nippes, Haiti, Earthquake*; US Geological Survey: Reston, VA, USA, 2021.
69. Wang, S.; Xu, C.; Li, Z.; Wen, Y.; Song, C. The 2018 Mw 7.5 Papua New Guinea Earthquake: A Possible Complex Multiple Faults Failure Event with Deep-Seated Reverse Faulting. *Earth Space Sci.* **2020**, *7*, e2019EA000966. [CrossRef]
70. Yin, F.; Lewis, P.E.; Gómez-Dans, J.L. Bayesian Atmospheric Correction over Land: Sentinel-2/Msi and Landsat 8/Oli. *Geosci. Model Dev.* **2022**, *15*, 7933–7976. [CrossRef]
71. Le Toan, T.; Beaudoin, A.; Riom, J.; Guyon, D. Relating forest parameters to SAR data. In Proceedings of the IGARSS'91 Remote Sensing: Global Monitoring for Earth Management, Espoo, Finland, 3–6 June 1991.
72. Suri, M. *Global Solar Atlas 2.0 Technical Report*; World Bank: Washington, DC, USA, 2019.
73. Google. The Global Precipitation Measurement Mission (Gpm). Available online: https://developers.google.com/earth-engine/datasets/catalog/NASA_GPM_L3_IMERG_V06 (accessed on 2 September 2023).
74. Google. Supervised Classification—The Classifier Package Handles Supervised Classification by Traditional Ml Algorithms Running in Earth Engine. Available online: https://developers.google.com/earth-engine/guides/classification (accessed on 15 February 2023).
75. Aksoy, S.; Yildirim, A.; Gorji, T.; Hamzehpour, N.; Tanik, A.; Sertel, E. Assessing the Performance of Machine Learning Algorithms for Soil Salinity Mapping in Google Earth Engine Platform Using Sentinel-2a and Landsat-8 Oli Data. *Adv. Space Res.* **2022**, *69*, 1072–1086. [CrossRef]
76. Al-Amri, S.S.; Kalyankar, N.V.; Khamitkar, S.D. A Comparative Study of Removal Noise from Remote Sensing Image. *arXiv* **2010**, arXiv:1002.1148.
77. Velez, D.R.; White, B.C.; Motsinger, A.A.; Bush, W.S.; Ritchie, M.D.; Williams, S.M.; Moore, J.H. A Balanced Accuracy Function for Epistasis Modeling in Imbalanced Datasets Using Multifactor Dimensionality Reduction. *Genet. Epidemiol. Off. Publ. Int. Genet. Epidemiol. Soc.* **2007**, *31*, 306–315. [CrossRef]
78. He, T.; Mu, S.; Zhou, H.; Hu, J. Wood Species Identification Based on an Ensemble of Deep Convolution Neural Networks. *Wood Res.* **2021**, *66*, 1–14.
79. Zhao, L.; Liu, J.; Peters, S.; Li, J.; Mueller, N.; Oliver, S. Learning Class-Specific Spectral Patterns to Improve Deep Learning-Based Scene-Level Fire Smoke Detection from Multi-Spectral Satellite Imagery. *Remote Sens. Appl. Soc. Environ.* **2024**, *34*, 101152. [CrossRef]
80. Chang, S.; Deng, Y.; Zhang, Y.; Wang, R.; Qiu, J.; Wang, W.; Zhao, Q.; Liu, D. An Advanced Echo Separation Scheme for Space-Time Waveform-Encoding Sar Based on Digital Beamforming and Blind Source Separation. *Remote Sens.* **2022**, *14*, 3585. [CrossRef]
81. Ma, Y.; Chen, S.; Ermon, S.; Lobell, D.B. Transfer Learning in Environmental Remote Sensing. *Remote Sens. Environ.* **2024**, *301*, 113924. [CrossRef]
82. Luo, L.; Wang, X.; Guo, H.; Lasaponara, R.; Shi, P.; Bachagha, N.; Li, L.; Yao, Y.; Masini, N.; Chen, F. Google Earth as a Powerful Tool for Archaeological and Cultural Heritage Applications: A Review. *Remote Sens.* **2018**, *10*, 1558. [CrossRef]
83. Masson-Delmotte, V.; Zhai, P.; Pirani, S.; Connors, C.; Péan, S.; Berger, N.; Caud, Y.; Chen, L.; Goldfarb, M.; Scheel Monteiro, P.M. IPCC, 2021: Summary for Policymakers. In *Climate Change 2021: The Physical Science Basis. Contribution of Working Group I to the Sixth Assessment Report of the Intergovernmental Panel on Climate Change*; IPCC: Geneva, Switzerland, 2021.
84. Altman, J.; Ukhvatkina, O.N.; Omelko, A.M.; Macek, M.; Plener, T.; Pejcha, V.; Cerny, T.; Petrik, P.; Srutek, M.; Song, J.-S. Poleward Migration of the Destructive Effects of Tropical Cyclones during the 20th Century. *Proc. Natl. Acad. Sci. USA* **2018**, *115*, 11543–11548. [CrossRef] [PubMed]
85. Bloemendaal, N.; de Moel, H.; Martinez, A.B.; Muis, S.; Haigh, I.D.; van der Wiel, K.; Haarsma, R.J.; Ward, P.J.; Roberts, M.J.; Dullaart, J.C. A Globally Consistent Local-Scale Assessment of Future Tropical Cyclone Risk. *Sci. Adv.* **2022**, *8*, eabm8438. [CrossRef]
86. Knutson, T.R.; Chung, M.V.; Vecchi, G.; Sun, J.; Hsieh, T.-L.; Smith, A.J. Climate Change Is Probably Increasing the Intensity of Tropical Cyclones. *Crit. Issues Clim. Chang. Sci. Sci. Brief Rev.* **2021**, 4570334. [CrossRef]